



## FINAL REPORT

Contract Number FA9550-09-C-0012

Dynamic Behavior of Nano-Sized Particles in Novel Energetic  
Materials for Space Propulsion

---

Thomas L. Jackson, University of Illinois  
Steven F. Son, Purdue University  
William A. Dick, IllinoisRocstar LLC

IllinoisRocstar LLC  
Enterprise Works Building, Suite 220  
60 Hazelwood Drive  
P.O. Box 3001  
Champaign, IL 61826-3001

20090930142

©2009 IllinoisRocstar LLC

## REPORT DOCUMENTATION PAGE

AFRL-SR-AR-TR-09-0301

The public reporting burden for this collection of information is estimated to average 1 hour per response, including the time for reviewing the data needed, and completing and reviewing the collection of information. Send comments regarding this burden estimate or any other aspect of this collection of information, including suggestions for reducing the burden, to the Department of Defense, Executive Service Directorate (0704-0188). Response to this collection of information is required by law (50 U.S.C. 1201) and will be subject to any penalty for failing to comply with a collection of information if it does not display a currently valid OMB control number.

PLEASE DO NOT RETURN YOUR FORM TO THE ABOVE ORGANIZATION.

1. REPORT DATE (DD-MM-YYYY) 11-08-2009		2. REPORT TYPE Final		3. DATES COVERED (From - To) Oct 2008 - Jul 2009	
4. TITLE AND SUBTITLE  Dynamic Behavior of Nano-sized Particles in Novel Energetic Materials for Space Propulsion				5a. CONTRACT NUMBER  FA9550-09-C-0012	
				5b. GRANT NUMBER	
				5c. PROGRAM ELEMENT NUMBER	
6. AUTHOR(S)  Jackson, Thomas L. Son, Steven F. Dick, William A.				5d. PROJECT NUMBER	
				5e. TASK NUMBER	
				5f. WORK UNIT NUMBER	
7. PERFORMING ORGANIZATION NAME(S) AND ADDRESS(ES)  IllinoisRocstar LLC 60 Hazelwood Drive P. O. Box 3001 Champaign, IL 61826-3001				8. PERFORMING ORGANIZATION REPORT NUMBER  IR2009-002	
9. SPONSORING/MONITORING AGENCY NAME(S) AND ADDRESS(ES)  AF Office of Scientific Research 875 N. Randolph St. Room 3112 Arlington, VA 22203				10. SPONSOR/MONITOR'S ACRONYM(S)  AFOSR	
				11. SPONSOR/MONITOR'S REPORT NUMBER(S)	
12. DISTRIBUTION/AVAILABILITY STATEMENT  Approved for Public Release; distribution unlimited.					
13. SUPPLEMENTARY NOTES  None.					
14. ABSTRACT We report a comprehensive computational and experimental program investigating the characteristics and dynamic behavior of nano-size aluminum in novel energetic materials. For the computational portion, we employed (i) our in-house packing code, Rocpack, to generate morphologies of interest for heterogeneous propellants; (ii) modified our solid rocket motor CFD code, Rocstar, to include appropriate models for chemistry, radiation, and nano-sized aluminum; and (iii) simulated transient behavior of the propellants at rocket motor conditions. For the experimental portion, we (i) used the mixing facility at Purdue University to prepare appropriate propellant samples containing nano-sized aluminum, thus allowing for a full characterization of the propellant (composition; particle size distribution) necessary for a coordinated modeling and experimental program; and (ii) carried out both steady and unsteady experiments to fully characterize the propellants. Our R&D program investigated the applicability of the Rocstar simulation framework for novel energetic high-density propellants, sought to establish the feasibility of an experimental validation program for these propellants, and provides a firm foundation for commercializing the simulation software. The simulations were performed at IllinoisRocstar LLC and the experiments were performed at Purdue.					
15. SUBJECT TERMS  Nanomaterials, propellants, simulation, particle packing, energetic materials, nano-aluminum.					
16. SECURITY CLASSIFICATION OF:			17. LIMITATION OF ABSTRACT	18. NUMBER OF PAGES	19a. NAME OF RESPONSIBLE PERSON
a. REPORT	b. ABSTRACT	c. THIS PAGE			William A. Dick
U	U	U	UU	45	19b. TELEPHONE NUMBER (Include area code) (217) 417-0885

## Executive Summary

We are developing a comprehensive computational and experimental program to investigate the characteristics and dynamic behavior of nano-size aluminum in novel energetic materials. Two classes of advanced propellants will be considered. The first will be composite propellants, consisting of solids including AP, HMX, RDX, or nano-aluminum with a suitable binder such as HTPB. The second will be a nanoscale aluminum and ice propellant. For the computational portion, we will (i) use our in-house packing code to generate morphologies of interest for heterogeneous propellants; (ii) modify our CFD code to include appropriate models for chemistry, radiation, and nano-sized aluminum; and (iii) simulate transient behavior of the propellants at rocket motor conditions. For the experimental portion, we will (i) use the mixing facility at Purdue to prepare appropriate propellant samples containing nano-sized aluminum, thus allowing for a full characterization of the propellant (composition; particle size distribution) necessary for a coordinated modeling and experimental program; and (ii) carry out both steady and unsteady experiments to fully characterize the propellants. The experiments will be carried out in a window pressure vessel rated to 6000 psi and in a small end-burning rocket motor. The experiments will also be used for model calibration and for validation.

This final report describes Phase 1 work on the computational modeling, validation, and propellant formulation. Initial results show excellent agreement with prior experimental data, as well as the path forward for the next steps of the work.

## 1 Introduction

This final report documents the status of initial work performed on STTR contract FA9550-09-C-0012, *Dynamic Behavior of Nano-Sized Particles in Novel Energetic Materials for Space Propulsion*. The outline of the report is as follows. We begin by restating the Phase I Technical Objectives and the Phase I Work Plan. In Section 2 we present a literature review of relevant work. In Section 3 we present, in its entirety, the mathematical model for nano-aluminum-based propellants. Although a portion of the model appears in [1], we felt it best to present a clear picture for future reference. Results are presented in Section 4. As part of Phase I funding, we performed a validation study in Section 4.1 by comparing burn rates from the model and simulations with those obtained from the experimental data of [2]. The effort involved generating a model for the morphology, modifying the radiation/combustion code, performing a grid resolution study, and then simulating the burn through of the model propellant for various pressures. We note that excellent agreement is obtained. In Section 4.2 we present preliminary results for a propellant manufactured at Purdue as part of Phase I funding. A more detailed presentation of the Purdue experimental results are given in Section 5.

### 1.1 Phase I Technical Objectives

Our research and development program investigated the applicability of our simulation framework for novel energetic high-density propellants, established the feasibility of an experimental validation program for these propellants, and provided a foundation for commercializing the simulation software. The simulations were performed at IllinoisRocstar LLC and the experiments were performed at Purdue. To this end our Phase I objectives were as follows:



1. Develop a matrix of propellant formulations by varying AP particle size, solids content (AP, HMX, RDX, nano-aluminum), pressure, initial propellant temperature;
2. Prepare samples with the mixing facility at Purdue;
3. Conduct preliminary burning rate experiments at pressures up to 6000 psi, measuring burning rate and using high-speed imaging and high-speed spectroscopy;
4. Conduct preliminary dynamic experiments of ignition under realistic rocket conditions in a windowed pressure vessel by a CO<sub>2</sub> laser;
5. Modify the current simulation code to include models for nitramines, nano-aluminum, radiation, and combustion. As discussed above, there is already in existence a substantial foundation for the work, but certain modifications will have to be made for the novel energetic propellants proposed here;

A number of these objectives were met in Phase 1.

## 1.2 Phase I Work Plan

Under Phase I STTR funding we firmly established the feasibility of using our simulation codes for the new class of propellant formulations proposed here. We also developed the experimental validation program, and planned the commercialization process for the engineering analysis product(s). In the remainder of this section, we will expand the description of the technical issues introduced in the previous section.

1. The computational approach employed our in-house packing code to create three-dimensional random packs of spheres that can represent the oxidizer and nitramines. The nano-sized aluminum is treated by homogenizing it with the binder to create a blend. The thermo-mechanical behavior (density, thermal conductivity, regression rate) is modeled using our homogenization strategies. The energetic consequences of the addition of nano-sized aluminum in the gas-phase combustion field is modeled by a radiation transport equation and by aluminum oxidation heat release.
2. The experimental approach, carried out at Purdue, focused on both steady and unsteady behavior of novel energetic propellants. After a complete matrix has been properly defined (AP, HMX, RDX, nano-aluminum, HTPB; with input from the sponsor or AFRL personnel), some samples were created by the mixing facility at Purdue as part of an overall feasibility study. Each sample is characterized with respect to composition and particle size distribution. This allowed for a coordinated effort between the modeling and the experiments. The samples are then placed in the windowed pressure vessel, where both the pressure and the initial temperature of the sample is varied. We note that most previously reported work on propellants focus mainly on pressure; here, we varied the initial temperature as part of the study matrix. The burning rate, high-speed imaging, and high-speed spectroscopy is obtained for the prepared samples.

## 2 Literature Review

Many factors are important when selecting propellant formulation in a solid motor system. Of special importance is the notion of internal ballistics, a category that encompasses propellant characteristics such as burn rate, physical properties, and burning surface phenomena. Furthermore, oxidizer, fuel, and binder selection will also affect other important design decisions such as specific impulse, ignitability, and aging. In the strive to maximize  $I_{sp}$  and increase propellant burn rates, designers have typically resorted to energetic catalysts, increased oxidizer loading, or reducing the oxidizer particle size [3]. In ammonium perchlorate, aluminum, and hydroxyl-terminated polybutadiene (AP/Al/HTPB) composite propellants, the primary topic of interest for this project, further optimization has also resulted in the use of bimodal coarse and fine AP distributions to modify flame kinematics and improve surface burning where the introduction of fine oxidizers generally result in an increase in burning rate [5]. Conversely, studies of propellant with decreasing micrometric aluminum sizes show only a marginal increase [14]. When transitioning to nano-scale aluminum particles, though, the drastically increased reactive surface area per unit mass results in completely different burning characteristics leading to reduced agglomeration, higher combustion temperature, and lower ignition delay [10], warranting further investigation. To accomplish a characterization of the dynamic behavior of AP/nAl composites, transient effects will be studied in Crawford bomb strand burners and a sub-scale rocket motor.

Before pursuing such endeavors it is first necessary to formulate an appropriate propellant test matrix based on existing work [2-5]. Doing so will allow verification of Purdue's mixing procedures and repeatability tests, which will then allow robust calibration for the CFD code being developed at IllinoisRocstar, LLC. For completion, a cursory overview of considerations in AP/Al formulation selection is presented in sections 2.1 and 2.2.

### 2.1 Ammonium Perchlorate

As stated earlier, the burn rate of a solid propellant can be increased by increasing the amount of loaded oxidizer, reducing the oxidizer particle size, or both. However, this can only go so far before manufacturing considerations put a constraint on maximum amount of allowable solids (typically anything higher than 90% solids cannot be mixed). To understand the role of AP size in propellants it is necessary to introduce the role of the leading edge flame (LEF) discussed by [9]. As an example, [5] compared the burn rate effects of AP and aluminum formulation at pressures up to 5000 psi where they concluded that direct replacement of  $\mu$ Al with nAl shows virtually no change when using monomodal AP. By contrast bimodal AP exhibited markedly different behavior over the entire pressure range.

Related to this is the  $\mu$ Al agglomeration sizes as studied by [4]. Here the authors discuss how large, monomodal AP creates oxidizer-rich regions which in turn results in unfavorable ignition conditions. Consequently the aluminum liquefies and accumulates before reacting resulting in increased slag formation and unburned fuel. The specifics however, are dependent on the ratio of fine to coarse AP as well as the selected sizes, but both [5] and [4] illustrate the need for bimodal AP to advantageously utilize nano-aluminum as an energetic replacement for micrometric-aluminum. In general, though, burn rate is most enhanced when the ratio of fAP to cAP is approximately 0.25 [11].

## 2.2 Nano-Aluminum

Many theories have been presented to explain the marked increase in burn rate when using nAl including the following:

1. Shortened ignition delay since less time is needed to heat a nanoparticle to ignition temperature [2];
2. Burning at the surface of the propellant results in additional conductive and radiative heat interaction [12];
3. Thermal expansion of nano-aluminum is enough to crack the non-reactive aluminum oxide coating, exposing unreacted aluminum [10];
4. Increased specific surface area results in more readily reactive surface atoms [10].

No matter the reason, the increased reactivity of nano-aluminum compared to micrometric aluminum requires additional attention to detail regarding storage, mixing, and ingredient compatibility. Despite the many types and origins of nAl available, only three will be considered due to their immediate availability at Purdue, as summarized in Table 1.

Table 1: Nano-Aluminum Inventory at Purdue

Manufacturer	Origin	Designation	Nominal Size [nm]	Comments
Argonide	Russia	ALEX	50	Uncoated
Argonide	Russia	L-ALEX	50	Palmitic Acid Coating
NovaCentrix	USA	N80	80	Uncoated

This recently acquired stock has not yet undergone SEM imaging for size distribution, BET analysis to determine the specific surface area, or hydrochloric acid decomposition to determine the percent active aluminum, but historical data in Table 2 indicates that the palmitic acid coating greatly increases the percent active aluminum, the ratio between aluminum and aluminum oxide,  $\text{Al}_2\text{O}_3$ , while the ALEX and N80 were noticeably lower. As emphasized by [7] the storage of uncoated nAl is extremely important as they were able to demonstrate a reduction of active aluminum in ALEX from 80% to 30% in seven days at accelerated conditions of 40°C and 75% relative humidity, and although Purdue raw stock is stored in an inert argon environment, cast propellant is stored at ambient conditions and may be subject to time-dependent aging and moisture absorption. In fact, a study using 100-150nm ALEX and 100-150nm C-ALEX (viton-A coated) showed that C-ALEX increased burn rate 126% over pure HTPB solid fuel, whereas the ALEX only yielded a 61% increase. Consequently, unnecessary exposure of either raw or cast nAl to the atmosphere is necessary to ensure repeatable mixes and results.

In addition, the high specific surface area,  $s$ , compared to [2] whose nAl typically had  $s < 15 \text{ m}^2/\text{g}$ , poses potential mixing problems since the viscosity of the uncured propellant increases drastically with  $s$ . Also, the high specific surface area also increases the nAl's likelihood of spontaneous reaction with either ambient moisture or oxidizing agents during casting. Both issues are documented in section 4.



Table 2: Historical nAl Characteristics (October 2007)

Designation	Average Particle Size [nm]	Specific Surface Area [m <sup>2</sup> /g]	Percent Active Aluminum
ALEX	n/a	n/a	74
L-ALEX	n/a	n/a	90
N80	80	25.7	77.7

### 3 Mathematical Model

#### 3.1 Radiative Transfer Equations

The cloud formed by the fine/ultrafine particles is modeled, from the radiative standpoint, as a gray medium with time-space varying emission and absorption characteristics. In this section the radiative heat transfer equation for the cloud will be derived. The derivation assumes that the propellant surface lies in the  $x - y$  plane and burns in the nominal  $z$ -direction.

The radiative transfer equation (RTE) for a gray medium is given by

$$\mathbf{s} \cdot \nabla I + (K_s + K_a)I = K_{em}I_b + \frac{K_s}{4\pi} \int_{4\pi} I \Phi d\Omega', \quad (1)$$

$$\nabla = \left( \frac{\partial}{\partial x}, \frac{\partial}{\partial y}, \frac{\partial}{\partial z} \right), \quad (2)$$

$$\int_{4\pi} d\Omega' = \int_{\phi'=0}^{2\pi} \int_{\theta'=0}^{\pi} \sin \theta' d\theta' d\phi', \quad (3)$$

where  $I = I(\mathbf{r}, \mathbf{s})$  is the intensity that depends on position and direction,  $\Phi = \Phi(\mathbf{s}, \mathbf{s}')$  the scattering phase function,  $\mathbf{r} = (x, y, z)$  the position vector, and  $\mathbf{s} = (s_x, s_y, s_z)$  the direction cosines

$$s_x = \sin \theta \cos \phi, \quad s_y = \sin \theta \sin \phi, \quad s_z = \cos \theta, \quad (4)$$

with  $0 \leq \theta \leq \pi$  the polar angle with respect to the  $z$ -axis,  $0 \leq \phi \leq 2\pi$  the azimuthal angle with respect in the  $x - y$  plane, and the blackbody intensity  $I_b$  is given by

$$I_b = \sigma T^4 / \pi, \quad (5)$$

with  $\sigma = 5.67 \times 10^{-12} \text{ W/cm}^2\text{K}^4$ , the Stefan-Boltzmann constant. The preceding parameters are the scattering coefficient  $K_s$ , the absorption coefficient  $K_a$ , and the total emission coefficient  $K_{em}$ .

The incident radiation  $G$  and the radiative heat flux vector  $\mathbf{q}$  are defined as

$$G(\mathbf{r}) = \int_{4\pi} I(\mathbf{r}, \mathbf{s}') d\Omega', \quad (6)$$

$$\mathbf{q}(\mathbf{r}) = \int_{4\pi} I(\mathbf{r}, \mathbf{s}') \mathbf{s}' d\Omega'. \quad (7)$$

Our model makes a number of assumptions:

1. The particulate-mixture cloud can be modeled as a gray medium; the radiative properties (absorption and scattering) are independent of the spectral wave number.

2. The propellant is opaque (i.e., the transmissivity  $\tau$  is zero).
3. We ignore in depth absorption at the surface.
4. The propellant surface is a diffuse-gray surface and, as such, it emits and reflects diffusely (i.e., the exiting intensity is independent of direction); then

$$I(\mathbf{r}_w, \mathbf{s}) = J_w(\mathbf{r}_w)/\pi, \quad \mathbf{n} \cdot \mathbf{s} > 0, \quad (8)$$

where

$$J_w = \epsilon\pi I_b + \hat{\rho}H \quad (9)$$

is the surface radiosity and the subscript  $w$  denotes a value on the propellant surface. Here,  $H$  is the hemispherical irradiation (i.e., incoming radiative heat flux)

$$H(\mathbf{r}_w) = \int_{\mathbf{n} \cdot \mathbf{s}' < 0} I(\mathbf{r}_w, \mathbf{s}') |\mathbf{n} \cdot \mathbf{s}'| d\Omega', \quad (10)$$

where  $\mathbf{n}$  is the local outward normal, and  $\mathbf{n} \cdot \mathbf{s}' = \cos \theta'$  is the cosine of the angle between any incoming direction  $\mathbf{s}'$  and the surface normal.

5. The intensity is periodic in the  $x$  and  $y$  directions (the propellant burns downward in the nominal  $-z$  direction).
6. The phase scattering function is taken to be linear-anisotropic

$$\Phi(\mathbf{s}, \mathbf{s}') = 1 + A_1 \mathbf{s} \cdot \mathbf{s}'. \quad (11)$$

Setting  $A_1 = 0$  implies isotropic scattering. However, Brewster and Parry [15] note that smoke is anisotropic and so we allow for this possibility.

Most, if not all, of the assumptions could be relaxed if more information about the radiation field is known. In any event, we wish to begin the model within the simplest possible framework.

To solve the radiative transfer equation (1) we use the  $P_1$  approximation of the spherical harmonics method, which is equivalent to the first moment method. We begin by writing for the intensity

$$I(\mathbf{r}, \mathbf{s}) = a(\mathbf{r}) + \mathbf{b}(\mathbf{r}) \cdot \mathbf{s}. \quad (12)$$

Substituting (12) into (6) and (7) yields the relations

$$G = 4\pi a, \quad \mathbf{q} = \frac{4\pi}{3} \mathbf{b}, \quad (13)$$

which in turn yields for the intensity

$$I(\mathbf{r}, \mathbf{s}) = \frac{1}{4\pi} [G(\mathbf{r}) + 3\mathbf{q}(\mathbf{r}) \cdot \mathbf{s}]. \quad (14)$$

In deriving these relations we used the following identities

$$\int_{4\pi} d\Omega' = 4\pi, \quad \int_{4\pi} \mathbf{s}' d\Omega' = 0, \quad \int_{4\pi} \mathbf{s}' \mathbf{s}' d\Omega' = \frac{4\pi}{3} \mathcal{I}, \quad (15)$$



where  $\mathcal{I}$  is the unit tensor. The integral on the right hand side of the RTE (1) then becomes

$$\int_{4\pi} I(\mathbf{r}, \mathbf{s}') \Phi(\mathbf{s}, \mathbf{s}') d\Omega' = G + A_1 \mathbf{q} \cdot \mathbf{s}. \quad (16)$$

Substituting the intensity (14) into (1), multiplying by  $(1, \mathbf{s})$ , respectively, and integrating each equation over all solid angles, yields the following two relations

$$\nabla \cdot \mathbf{q} = 4\pi K_{em} I_b - K_a G =: R, \quad (17)$$

$$\nabla G = -(K_s + K_a)[3 - A_1 \omega] \mathbf{q} =: P \mathbf{q}, \quad (18)$$

where  $\omega = K_s/(K_s + K_a)$  is the albedo. These last two relations can be combined to yield a single equation for  $G$  in conservative form:

$$\nabla^2 G - \frac{\nabla P \cdot \nabla G}{P} = P R. \quad (19)$$

This equation, subject to appropriate boundary conditions that will be defined below, is to be solved numerically in the gas-phase together with the zero Mach number reactive equations. Once  $G$  is known, the radiative heat flux is given by

$$\mathbf{q} = \frac{-1}{(K_s + K_a)(3 - A_1 \omega)} \nabla G, \quad (20)$$

and in the energy equation we have

$$\nabla \cdot \mathbf{q} = 4\pi K_{em} I_b - K_a G. \quad (21)$$

(See the discussion in Modest [16], page 512.)

For the boundary condition at the propellant surface, we require that such a boundary condition is satisfied in an integral sense (see the discussion in Modest [16], p. 470). The analysis starts by writing for the intensity along the propellant surface:

$$I(\mathbf{r} = \mathbf{r}_w, \mathbf{s}) = I_w(\mathbf{r}_w, \mathbf{s}), \quad (22)$$

for  $\mathbf{n} \cdot \mathbf{s} > 0$  (i.e., the intensity leaving a surface must be prescribed in some fashion for all outgoing directions  $\mathbf{n} \cdot \mathbf{s} > 0$ ). This relation is, of course, general in that it applies in all cases. Using assumption 4, that the surface emits and reflects diffusely, the preceding reduces to

$$I(\mathbf{r} = \mathbf{r}_w, \mathbf{s}) = I_w(\mathbf{s}), \quad \text{for } \mathbf{n} \cdot \mathbf{s} > 0. \quad (23)$$

Evaluating (14) on the surface, multiplying by  $\mathbf{s} \cdot \mathbf{n}$  and integrating over the hemisphere, yields

$$\int_{\mathbf{n} \cdot \mathbf{s} > 0} I_w(\mathbf{s}) \mathbf{s} \cdot \mathbf{n} d\Omega = \frac{1}{4\pi} \int_{\mathbf{n} \cdot \mathbf{s} > 0} (G + 3\mathbf{q} \cdot \mathbf{s}) \mathbf{s} \cdot \mathbf{n} d\Omega. \quad (24)$$

Let

$$\mathbf{q} \cdot \mathbf{s} = q_{t1} \sin \theta \cos \phi + q_{t2} \sin \theta \sin \phi + q_n \cos \theta, \quad (25)$$

where  $(q_{t1}, q_{t2})$  are the tangent components and  $q_n$  the normal component, and recall that  $\mathbf{s} \cdot \mathbf{n} = \cos \theta$ . Substitution yields

$$\int_{\mathbf{n} \cdot \mathbf{s} > 0} I_w(\mathbf{s}) \mathbf{s} \cdot \mathbf{n} d\Omega = \frac{1}{4}(G + 2q_n), \quad (26)$$

or,

$$G + 2q_n = 4 \int_{\mathbf{n} \cdot \mathbf{s} > 0} I_w(\mathbf{s}) \mathbf{s} \cdot \mathbf{n} d\Omega. \quad (27)$$

Substituting assumption 4 for the intensity in terms of the surface radiosity yields

$$G + 2q_n = 4J_w. \quad (28)$$

In addition to this relation, we require that the normal radiative heat flux is the sum of the incident and reflected (radiosity) contributions:

$$q_n = J_w - H. \quad (29)$$

The incident radiation is eliminated in favor of the radiosity using (9) and the hemispherical reflectivity is related to the absorptivity  $\alpha$  by the Kirchhoff law for diffuse-gray surfaces,

$$\hat{\rho} = 1 - \alpha, \quad (30)$$

to yield

$$q_n = \frac{\epsilon \pi I_b - \alpha J_w}{1 - \alpha}. \quad (31)$$

We use (28) and (31) to eliminate  $J_w$ , yielding

$$2q_n = \frac{1}{2 - \alpha} [4\epsilon \pi I_b - \alpha G]. \quad (32)$$

Substituting (20) to eliminate  $\mathbf{q}$  yields the proper boundary condition along the propellant surface

$$\frac{-2\mathbf{n} \cdot \nabla G}{(K_s + K_a)(3 - A_1 \omega)} = \frac{1}{2 - \alpha} [4\epsilon \pi I_b - \alpha G]. \quad (33)$$

This is an implicit boundary condition for the unknown function  $G$  (i.e., a Robin boundary condition).

The other boundary conditions assume either periodicity for randomly packer propellants or zero normal fluxes for sandwich propellants.  $G$  is periodic at

$$x = \pm L_x, \quad y = \pm L_y, \quad (34)$$

$$\frac{\partial G}{\partial x} = 0 \quad \text{at } x = \pm L_x, \quad \frac{\partial G}{\partial y} = 0 \quad \text{at } y = \pm L_y, \quad (35)$$

and far away from the propellant surface the radiation field is in equilibrium

$$\mathbf{q} \rightarrow 0, \quad \text{i.e., } \nabla G = 0 \quad \text{as } z \rightarrow \infty. \quad (36)$$

To summarize, we solve (19) for the incident radiation  $G$ , subject to the boundary conditions (33-36). Once  $G$  has been determined, the radiative heat flux  $\mathbf{q}$  can be found from (20). The unknown parameters that must be modeled are  $K_s$ ,  $K_a$ ,  $K_{em}$ ,  $A_1$ ,  $\alpha$ , and  $\epsilon$ .

### 3.2 Governing Equations

Radiation affects the combustion field through the radiative heat contribution,  $\nabla \cdot \mathbf{q} \equiv -\nabla \cdot \mathbf{q}_r$ , and it affects the connection conditions at the propellant surface because of the term  $q_n$  in (31). The propellant surface is considered to be an opaque surface, in the sense that no radiation penetrates into the solid phase (i.e., all is absorbed at the surface). Thus, no changes are necessary to the solid-phase heat conduction equation. We note, however, that the presence of aluminum does affect the heat conduction in the solid, mainly because of changes in thermal conductivity of the aluminum fuel blend. This effect is accounted for by using homogenization formulas as discussed by Jackson *et al.* [17]. These formulas will be described in more detail below.

#### 3.2.1 Gas Phase

In this section we briefly outline the gas-phase equations to highlight the changes due to the presence of the radiative field.

Consider a reacting mixture composed of  $N_s$  species that can react according to  $N_r$  reaction steps. Let  $T$  denote the gas-phase temperature and  $Y_i$ ,  $i = 1, \dots, N_s$ , the gas-phase species mass fractions. The equations expressing conservation of energy and species mass in a non-conservative form are

$$\rho c_p \frac{DT}{Dt} - \frac{dP_0}{dt} = -\nabla \cdot \mathbf{q} + \sum_{i=1}^{N_r} \alpha_i R_i, \quad (37)$$

$$\rho \frac{DY_k}{Dt} = \nabla \cdot \left( \frac{\lambda}{c_p} \nabla Y_k \right) + \sum_{i=1}^{N_r} \beta_{k,i} R_i, \quad k = 1, \dots, N_s, \quad (38)$$

where  $\beta_{k,i}$  and  $\alpha_i$  are coefficients based upon mass and total enthalpy conservation, respectively, that are fully determined given a particular reaction scheme. The reaction steps are expressed in general form as

$$R_i = D_{g,i} P_0^{n_i} T^{m_i} \prod_{k=1}^{N_s} Y_k^{\nu_{i,k}} \exp(-\theta_i/T), \quad (39)$$

where  $D_{g,i}$  is the gas-phase Dankohler number for species  $i$ ;  $P_0$  is the leading order pressure in a small Mach number expansion and can, at most, be a function of time; and  $\theta_i$  the gas-phase activation temperature for species  $i$ . For global kinetics, the species exponent,  $\nu_{i,k}$ , in the reaction rates need not be related to the stoichiometric coefficients of the corresponding reaction; their values are assigned by matching reaction rate constants with experiments. The parameters of the combustion model ( $D_{g,i}$ ,  $n_i$ ,  $m_i$ ,  $\nu_{i,k}$ , and  $\theta_i$ ) are calibrated using a global optimization strategy discussed by Massa *et al.* [18]. The values of the combustion model parameters are identical to those reported in Jackson *et al.* [17].

In addition,  $\rho$  is the gas-phase density,  $c_p$  the specific heat assumed to be independent of the composition,  $\lambda$  the gas-phase thermal conductivity taken to be a function of the temperature and the volume fraction of aluminum and aluminum oxide ( $\text{Al}_2\text{O}_3$ ) in the gas-phase, and  $\mathbf{q}$  the heat-flux vector. In writing down these equations the Lewis number for each species was assumed to be unity, and second-order or higher terms in the Mach number were neglected. The heat-flux vector is the sum of a conductive part and a radiative part,

$$\mathbf{q} = \mathbf{q}_c + \mathbf{q}_r, \quad (40)$$



where the conductive part is assumed to obey Fourier's law

$$\mathbf{q}_c = -\lambda \nabla T, \quad (41)$$

and the radiative part is given in the previous section

$$\mathbf{q}_r = \frac{-1}{(K_s + K_a)(3 - A_1 \omega)} \nabla G, \quad (42)$$

and

$$\nabla \cdot \mathbf{q}_r = 4\pi K_{em} I_b - K_a G. \quad (43)$$

Recall that  $I_b$  is the black body radiation

$$I_b = \frac{\sigma}{\pi} T^4, \quad (44)$$

and the incident radiation term  $G$  is governed by the equation (19).

The pressure,  $P$ , is written as the sum of two contributions, a leading-order term and a contribution of order  $O(M^2)$  where  $M$  is the Mach number,

$$P = P_0 + p, \quad \frac{p}{P_0} = O(M^2). \quad (45)$$

The leading-order term  $P_0$  is also called the thermodynamic pressure, and the second term  $p$  is called the hydrodynamic pressure. The Navier-Stokes momentum equation then becomes

$$\begin{aligned} \nabla P_0 = 0 &\Rightarrow P_0 = P_0(t), \\ \rho \frac{D\mathbf{u}}{Dt} &= \nabla \cdot \underline{\underline{\sigma}}, \end{aligned} \quad (46)$$

where  $\mathbf{u} = (u, v, w)$  are the velocity components, the mean pressure  $P_0$  is at most a function of time, and  $\underline{\underline{\sigma}}$  is the total stress tensor, the sum of the hydrodynamic pressure and viscous stress tensors,

$$\underline{\underline{\sigma}} = - \left( p + \frac{2}{3} \mu \nabla \cdot \mathbf{u} \right) \underline{\underline{I}} + \mu \left( \nabla \mathbf{u} + (\nabla \mathbf{u})^\top \right), \quad (47)$$

where  $\underline{\underline{I}}$  is the identity tensor,  $\mu$  is the gas-phase viscosity and is related to the gas-phase thermal conductivity via  $\mu = Pr\lambda/c_p$ , and the superscript  $\top$  denotes the matrix transpose. A constant value for the Prandtl number,  $Pr = 0.72$ , is assumed.

The continuity equation is

$$\frac{D\rho}{Dt} + \rho \nabla \cdot \mathbf{u} = 0, \quad (48)$$

and the equation of state reads

$$P_0 = \frac{\rho R_u T}{M_W}, \quad (49)$$

where  $R_u$  is the universal gas constant and  $M_W$  is the averaged molecular weight of the gas.

Although our code can include the Navier-Stokes equations, in this work we use the Oseen approximation which significantly reduces the computational burden, and calculations for sandwich propellants attest to its accuracy [19]. The Oseen approximation sets the mass flux nominally

normal to the burning surface to a constant and the mass flux nominally tangent to the surface to zero, thus satisfying the continuity but jettisoning the momentum equation. An alternative and essentially equivalent formulation is to set the density to a constant, so that the equation of state, Charles's law, is jettisoned; and a uniform velocity field  $u = 0$  and  $v = \text{constant}$  is adopted, which satisfies both the continuity equation and the momentum equation. Then the mass flux  $\rho v$  is constant, and the model is merely a variation on that proposed by Burke and Schumann in 1928 [20]. This approximation has proven to be adequate and suffices for our purposes here.

### 3.2.2 Solid Phase

If the effects of mechanical stress are neglected, and if condensed phase reactions are neglected in lieu of a reaction sheet at the surface, the solid phase can be characterized by its temperature field. The temperature distribution,  $T_c$ , inside the solid phase is governed by

$$\rho_c c_p \frac{\partial T_c}{\partial t} = \nabla \cdot (\lambda_c \nabla T_c), \quad (50)$$

where  $\rho_c$  is the density of the solid,  $c_p$  the specific heat assumed to be equal in the gas-phase, and  $\lambda_c$  the solid phase thermal conductivity. The density and thermal conductivity are functions of the spatial coordinates and are related to the propellant morphology by means of a particle marker method

$$\rho_c = \begin{cases} \rho_{AP} & \lambda_c = \begin{cases} \lambda_{AP} & \psi = 1 \\ \lambda_{blend} & \psi = -1, \end{cases} \\ \rho_{blend} \end{cases} \quad (51)$$

where  $\psi(x, y, z)$  is a particle marker flag such that a point  $(x, y, z)$  lies in the AP if  $\psi = 1$ , and in the blend if  $\psi = -1$ . The blend can be a homogenized mix of aluminum, AP, and binder. The density of the blend is then given by

$$\rho_{blend} = t_{AP}\rho_{AP} + t_{Al}\rho_{Al} + t_B\rho_B, \quad (52)$$

where  $\rho_{AP} = 1.95$  gm/cc is the density of AP,  $\rho_{Al} = 2.70$  gm/cc is the density of the aluminum,  $\rho_B = 0.92$  gm/cc is the density of binder, and  $t_i$  ( $i = AP, Al, B$ ) is the volume fraction of the blend that is the component  $i$ . Here,  $t_{AP} + t_{Al} + t_B = 1$ .

### 3.2.3 Pyrolysis Laws

The pyrolysis laws for AP and binder are given by the forms

$$r_{b,AP} = A_{AP} e^{-E_{AP}/R_u T_s}, \quad r_{b,B} = A_B e^{-E_B/R_u T_s}, \quad (53)$$

where  $T_s$  is the local surface temperature. Since aluminum does not have a pyrolysis law, for the blend we take

$$r_{b,blend} = A_{blend} e^{-E_{blend}/R_u T_s}, \quad (54)$$

where

$$A_{blend} = (A_{AP})^{t_{AP}} (A_B)^{t_B}, \quad E_{blend} = t_{AP}E_{AP} + t_B E_B, \quad (55)$$

with  $t_{AP} + t_{Al} + t_B = 1$ . It is not possible at this time to verify the correctness of (54) and (55) since a fully functional three-dimensional code with discrete aluminum is not complete, and so we use these relations with some reservations. We hope to return to this point at a later date.

### 3.2.4 Propagation of the Surface

Suppose the surface is defined by

$$\eta(x, y, z, t) = 0. \quad (56)$$

A point on the surface moves along the normal, and  $\eta$  does not change for such a point, so that

$$\frac{D\eta}{Dt} = 0, \quad \text{or} \quad \eta_t + \mathbf{v} \cdot \nabla \eta = 0, \quad \mathbf{v} = \left( \frac{dx}{dt}, \frac{dy}{dt}, \frac{dz}{dt} \right). \quad (57)$$

The normal, pointing into the gas, is

$$\mathbf{n} = \frac{\nabla \eta}{|\nabla \eta|}, \quad (58)$$

and the speed of the surface regression  $r_b$  ( $> 0$ ) is related to  $\mathbf{v}$  and  $\mathbf{n}$  by

$$\mathbf{v} = -r_b \mathbf{n}, \quad |\mathbf{v}| = r_b; \quad (59)$$

$r_b = r_b(x, z, t)$  is the local burning rate of the solid. Then (57) is

$$\eta_t - r_b \mathbf{n} \cdot \nabla \eta = 0, \quad (60)$$

or

$$\eta_t - r_b |\nabla \eta| = 0. \quad (61)$$

This is the kinematic equation that governs the propagation of the surface.

### 3.2.5 Connection Conditions

The connection conditions at the propellant surface relate the solution in the solid phase to that in the gas phase. The burning interface is treated as a reacting regressing sheet separating the two phases. The temperature, the normal mass flux, and the tangential velocity are continuous across the sheet, so that if  $\mathbf{n}$  is the surface normal pointing into the gas,

$$[T] = 0, \quad (62)$$

$$[M] = [\rho(\mathbf{u} \cdot \mathbf{n} + r_b)] = 0, \quad (63)$$

$$[\mathbf{u} \times \mathbf{n}] = 0. \quad (64)$$

The energy balance and the species mass balance across the interface become

$$[-\mathbf{n} \cdot \mathbf{q}] = -Q_s M, \quad (65)$$

$$\left[ \frac{\lambda}{c_p} \mathbf{n} \cdot \nabla Y_i \right] = M[Y_i]. \quad (66)$$

The jump operator in the above equations is defined as  $[\cdot] = (\cdot)_g - (\cdot)_c$ . If we eliminate the heat flux vector in the energy balance in terms of the corresponding conductive and radiative parts, then we get

$$[\lambda \mathbf{n} \cdot \nabla T] = \mathbf{n} \cdot \mathbf{q}_r|_g - Q_s M, \quad (67)$$



or, upon using (32),

$$[\lambda \mathbf{n} \cdot \nabla T] = \frac{1}{2(2 - \alpha)} (4\epsilon\pi I_b - \alpha G) - Q_s M. \quad (68)$$

We note that the phase-change heat release,  $Q_s$ , is a function of space along the surface according to

$$Q_s = \begin{cases} Q_{s,AP} & \psi = 1 \\ Q_{s,blend} & \psi = -1. \end{cases} \quad (69)$$

For the blend we have

$$Q_{s,blend} = w_{AP} Q_{s,AP} + w_{Al} Q_{s,Al} + w_B Q_{s,B}, \quad (70)$$

where  $w_i$  ( $i = AP, Al, B$ ) are the weight fractions of the blend that is the component  $i$ . Here,  $w_{AP} + w_{Al} + w_B = 1$ . Since aluminum does not pyrolyze, we set  $Q_{s,Al} = 0$ .

### 3.2.6 Coordinate Mapping

*Rocfire* uses a mapping that maps the non-flat moving interface onto a computational stationary flat plane. If we assume the surface to be single-valued, then we use

$$\eta = y - f(x, z, t). \quad (71)$$

The normal and tangent vectors at the surface are given by

$$\mathbf{n} = \frac{(-f_x, 1, -f_z)}{\sqrt{1 + f_x^2 + f_z^2}}, \quad \mathbf{t}_1 \cdot \mathbf{n} = 0, \quad \mathbf{t}_2 = \mathbf{n} \times \mathbf{t}_1, \quad (72)$$

with the constraints

$$|\mathbf{t}_1| = |\mathbf{t}_2| = 1. \quad (73)$$

Derivatives in the transformed space are replaced in the following fashion

$$\begin{aligned} \frac{\partial}{\partial x} &\rightarrow \frac{\partial}{\partial x} - f_x \frac{\partial}{\partial \eta}, \\ \frac{\partial}{\partial y} &\rightarrow \frac{\partial}{\partial \eta}, \\ \frac{\partial}{\partial z} &\rightarrow \frac{\partial}{\partial z} - f_z \frac{\partial}{\partial \eta}, \\ \frac{\partial}{\partial t} &\rightarrow \frac{\partial}{\partial t} - f_t \frac{\partial}{\partial \eta}, \\ \frac{D}{Dt} &\rightarrow \frac{\partial}{\partial t} + u \frac{\partial}{\partial x} + \bar{v} \frac{\partial}{\partial \eta} + w \frac{\partial}{\partial z}, \end{aligned} \quad (74)$$

where

$$\bar{v} = v - u f_x - w f_z - f_t, \quad (75)$$

and

$$\nabla^2 \rightarrow \frac{\partial^2}{\partial x^2} + (1 + f_x^2 + f_z^2) \frac{\partial^2}{\partial \eta^2} + \frac{\partial^2}{\partial z^2} - 2f_x \frac{\partial^2}{\partial x \partial \eta} - 2f_z \frac{\partial^2}{\partial z \partial \eta} - (f_{xx} + f_{zz}) \frac{\partial}{\partial \eta}. \quad (76)$$

Note that  $v$  is now eliminated as a dependent variable in favor of  $\bar{v}$ , and the boundary condition (64) can be rewritten as

$$u = -f_x \left( \frac{\bar{v} + wf_z + f_t}{1 + f_x^2} \right), \quad w = -f_z \left( \frac{\bar{v} + uf_x + f_t}{1 + f_z^2} \right). \quad (77)$$

In the Oseen approximation we set  $u = w = 0$  and so  $\bar{v} = -f_t$ .

### 3.2.7 Grid Stretching

It is convenient to first reflect the solid domain about the  $\eta = 0$  plane so that all equations are defined on the domain  $\eta > 0$ . Once this has been done, an additional grid stretching mapping can be used to cluster the computational points in the  $\eta$ -direction near the surface. The grid clustering mapping is given by the functional relationship  $\bar{\eta} = \bar{\eta}(\eta)$ . Then

$$\frac{\partial}{\partial \eta} \rightarrow \frac{d\bar{\eta}}{d\eta} \frac{\partial}{\partial \bar{\eta}}, \quad (78)$$

and

$$\frac{\partial^2}{\partial \eta^2} \rightarrow \left( \frac{d\bar{\eta}}{d\eta} \right)^2 \frac{\partial^2}{\partial \bar{\eta}^2} + \frac{d^2 \bar{\eta}}{d\eta^2} \frac{\partial}{\partial \bar{\eta}}. \quad (79)$$

*Rocfire* currently uses the mapping

$$\eta = \frac{\bar{\eta}}{[2 - (\bar{\eta}/L_\eta)^2]^C}, \quad (80)$$

where  $L_\eta$  is the end of the computational domain in the  $\eta$ -direction, and  $C$  is a clustering constant. Typically we choose  $C = 6$ .

### 3.2.8 Transformed Equations

In this section we summarize the equations and boundary conditions in the transformed  $(x, \bar{\eta}, z)$  space, with  $0 \leq \bar{\eta} < +\infty$ .

$\bar{\eta} > 0$

For the temperature, species, and radiation equation we have

$$\rho c_p \left( T_t + uT_x + \bar{v} \frac{d\bar{\eta}}{d\eta} T_{\bar{\eta}} + wT_z \right) - \frac{dP_0}{dt} = \bar{\nabla} \cdot (\lambda \bar{\nabla} T) - (4\pi K_{em} I_b - K_a G) + \sum_{i=1}^{N_r} \alpha_i R_i, \quad (81)$$

$$\rho \left( Y_{k,t} + uY_{k,x} + \bar{v} \frac{d\bar{\eta}}{d\eta} Y_{k,\bar{\eta}} + wY_{k,z} \right) = \bar{\nabla} \cdot \left( \frac{\lambda}{c_p} \bar{\nabla} Y_k \right) + \sum_{i=1}^{N_r} \beta_{k,i} R_i, \quad k = 1, \dots, N_s, \quad (82)$$

$$\begin{aligned} & G_{xx} + (1 + f_x^2 + f_z^2) \left( \frac{d^2 \bar{\eta}}{d\eta^2} G_{\bar{\eta}} + \left( \frac{d\bar{\eta}}{d\eta} \right)^2 G_{\bar{\eta}\bar{\eta}} \right) + G_{zz} \\ & - \frac{d\bar{\eta}}{d\eta} (2f_x G_{x\bar{\eta}} + 2f_z G_{z\bar{\eta}} + (f_{xx} + f_{zz}) G_{\bar{\eta}}) = (K_s + K_a)(3 - A_1 \omega) [K_a G - 4\pi K_{em} I_b], \end{aligned} \quad (83)$$

where

$$\begin{aligned} \bar{\nabla} \cdot (\lambda \bar{\nabla} T) &= (1 + f_x^2 + f_z^2) \left( \frac{d^2 \bar{\eta}}{d\eta^2} (\lambda T_{\bar{\eta}}) + \left( \frac{d\bar{\eta}}{d\eta} \right)^2 (\lambda T_{\bar{\eta}})_{\bar{\eta}} \right) \\ &+ (\lambda T_x)_x + (\lambda T_z)_z - \frac{d\bar{\eta}}{d\eta} (f_x (\lambda T_{\bar{\eta}})_x + f_x (\lambda T_x)_{\bar{\eta}} + f_z (\lambda T_{\bar{\eta}})_z + f_z (\lambda T_z)_{\bar{\eta}}), \end{aligned} \quad (84)$$

and similarly for the species  $Y_k$ .

For the fluid equations, they remain unchanged due to radiation, so they are not repeated here.

For the condensed phase temperature we have

$$\begin{aligned} \rho_c c_p \left( T_{c,t} + f_t \frac{d\bar{\eta}}{d\eta} T_{c,\bar{\eta}} \right) &= (1 + f_x^2 + f_z^2) \left( \frac{d^2 \bar{\eta}}{d\eta^2} (\lambda_c T_{c,\bar{\eta}}) + \left( \frac{d\bar{\eta}}{d\eta} \right)^2 (\lambda_c T_{c,\bar{\eta}})_{\bar{\eta}} \right) \\ &+ (\lambda_c T_{c,x})_x + (\lambda_c T_{c,z})_z + \frac{d\bar{\eta}}{d\eta} (f_x (\lambda_c T_{c,\bar{\eta}})_x + f_x (\lambda_c T_{c,x})_{\bar{\eta}} + f_z (\lambda_c T_{c,\bar{\eta}})_z + f_z (\lambda_c T_{c,z})_{\bar{\eta}}). \end{aligned} \quad (85)$$

Note that (85) is the equation used in our *Rocburn* code.

$\bar{\eta} \rightarrow \infty$

$$\frac{\partial}{\partial \bar{\eta}}(\cdot) = 0, \quad T_c = T_0, \quad (86)$$

where  $T_0$  is the cold supply temperature deep in the solid phase, and the notation  $(\cdot)$  means the quantities  $(T_g, T_c, Y_i, u, \bar{v}, w, p)$ .

$\bar{\eta} = 0$

$$f_t + r_b \sqrt{1 + f_x^2 + f_z^2}, \quad (87)$$

$$T(x, 0, z, t)|_g = T(x, 0, z, t)|_c, \quad (88)$$

$$\rho_g \bar{v} = \rho_c r_b \sqrt{1 + f_x^2 + f_z^2} = M \sqrt{1 + f_x^2 + f_z^2}, \quad (89)$$

$$u = -f_x \left( \frac{\bar{v} + w f_z + f_t}{1 + f_x^2} \right), \quad w = -f_z \left( \frac{\bar{v} + u f_x + f_t}{1 + f_z^2} \right). \quad (90)$$

$$\begin{aligned} \lambda_g \left( -f_x T_x + (1 + f_x^2 + f_z^2) \frac{d\bar{\eta}}{d\eta} T_{\bar{\eta}} - f_z T_z \right) \Big|_g &+ \lambda_c \left( f_x T_x + (1 + f_x^2 + f_z^2) \frac{d\bar{\eta}}{d\eta} T_{\bar{\eta}} + f_z T_z \right) \Big|_c \\ &= \left( \frac{1}{2(2 - \alpha)} (4\epsilon \pi I_b - \alpha G) - Q_s M \right) \sqrt{1 + f_x^2 + f_z^2}, \end{aligned} \quad (91)$$

$$\frac{\lambda_g}{c_p} \left( -f_x Y_{i,x} + (1 + f_x^2 + f_z^2) \frac{d\bar{\eta}}{d\eta} Y_{i,\bar{\eta}} - f_z Y_{i,z} \right) \Big|_g = M \left( Y_{i|g} - Y_{i,s} \right) \sqrt{1 + f_x^2 + f_z^2}, \quad (92)$$

$$\begin{aligned} \frac{-2(2 - \alpha)}{(K_s + K_a)(3 - A_1 \omega)} \left( -f_x G_x + (1 + f_x^2 + f_z^2) \frac{d\bar{\eta}}{d\eta} G_{\bar{\eta}} - f_z G_z \right) \Big|_g \\ = (4\epsilon \pi I_b - \alpha G)|_g \sqrt{1 + f_x^2 + f_z^2}, \end{aligned} \quad (93)$$

where  $Y_{i,s}$  denote fix surface values.



$$x = \pm L_x, z = \pm L_z$$

Periodicity.

### 3.3 Radiation Parameters

The radiation model is an adaption of the model used by Brewster and Parry [15] for conventional size aluminum, and used in our previous study of a blend of fine AP and aluminum [17]. Thus the contribution of the particles is accounted for by setting,

$$\begin{aligned} K_a &= \frac{3t_{\text{oxide}}\alpha_{\text{oxide}}}{D_{\text{oxide}}} + k_1 \frac{3t_{\text{Al}}\alpha_{\text{Al}}}{D_{\text{Al}}}, \\ K_s &= \frac{3t_{\text{oxide}}\hat{\rho}_{\text{oxide}}}{D_{\text{oxide}}} + k_1 \frac{3t_{\text{Al}}\hat{\rho}_{\text{Al}}}{D_{\text{Al}}}, \\ K_{em} &= \frac{3t_{\text{oxide}}\epsilon_{\text{oxide}}}{D_{\text{oxide}}} + k_1 \frac{3t_{\text{Al}}\epsilon_{\text{Al}}}{D_{\text{Al}}}, \end{aligned} \quad (94)$$

where  $t_{\text{Al}}$  and  $t_{\text{oxide}}$  are the volume fractions of aluminum and aluminum oxide, respectively, in the gas-phase;  $\alpha$ ,  $\hat{\rho}$ , and  $\epsilon$  are the absorptivity, reflectivity, and emissivity, respectively; and  $k_1$  is an empirical constant that reflects uncertainties in the evaluation of the diameter of the aluminum particles. In the simulations discussed in this paper, this parameter has been set to unity.

The average diameter of the injected particles can be much larger than the average diameter of the initial distribution of aluminum due to the possibility of agglomeration. Agglomeration is a phenomenon that depends on the aluminum particles surface residence time, which in turn depends on the propellant burn rate [21]. For burn rates typical of composite propellant with ultrafine aluminum, the residence time is short and agglomeration effects must be considered negligible. The experimental investigation of Stephens *et al.* [5] has shown that changing the size of aluminum from 3 microns to nano-size aluminum does not alter the burn rate for monomodal 200  $\mu\text{m}$  diameter AP. However, the addition of 36- $\mu\text{m}$  aluminum sharply reduces the propellant burn rate when the overall volume fraction of metal is maintained constant. Consequently, all simulations discussed in this work assume that the initial diameter of the particle ejected in the gas phase is  $D_0 = 3\text{-}\mu\text{m}$  corresponding to the upper boundary of the fine/ultrafine range as it was defined in the introduction.

Other model uncertainties include the values of  $\alpha_{\text{Al}}$ ,  $\hat{\rho}_{\text{Al}}$ , and  $\epsilon_{\text{Al}}$ , as well as the diameter  $D_{\text{oxide}}$ . The values of the constants used in this study are given in table (3), and are taken from Brewster and Parry [15]. The diameter of aluminum and oxide particles are determined by solving for Eulerian fields representative of the dispersed gas-particulate mixture; this topic is discussed in detail in the next section.

The parameters listed in equation (94) are identical to those used by Jackson *et al.* [17] and consider the contribution of the particles only. The contribution of the gas mixture is accounted for by evaluating the effective absorption coefficient for the gray gas as the Planck-mean absorption coefficient,  $K_{p,gas}$ , Modest [16], page 344.  $K_{p,gas}$  should be in principle determined by integrating the spectral absorption coefficient of the gas over the relevant bands. The result of this calculation would be temperature, pressure and composition dependent. Due to the absence of a detailed kinetic mechanism in our model, only the pressure dependence is retained,

$$K_{p,gas} = \kappa_{p,gas}P. \quad (95)$$

Assuming the combustion products to be composed in large part of  $CO_2$ , we select the value  $\kappa_{p,gas} = 0.3 \text{ cm}^2 \text{ atm}^{-1}$ , based upon the results of Zhang and Modest [22]. For the gas-particulate mixture, the coefficients are determined by augmenting  $K_a$  and  $K_{em}$  in equation (94) by the contribution  $K_{p,gas}$ .

	$\alpha$	$\hat{\rho}$	$\epsilon$	$D \text{ (}\mu\text{m)}$
Al	0.10	0.90	1.00	1.0
Al <sub>2</sub> O <sub>3</sub>	0.45	0.55	0.45	0.3

Table 3: Radiation parameter values; from Brewster and Parry [15].

### 3.4 Aluminum Modeling

The presence of aluminum in the solid phase is accounted for by evaluating the density, thermal conductivity, and pyrolysis rate according to homogenization formula derived for fine binder-aluminum blend. Most of the homogenization formulae are dictated by conservation principles, and their derivation is straightforward. The expression for the thermal conductivity does not stem from a conservation argument. The formulae used in this research are identical to those described by Jackson *et al.* [17],

$$1 = (1 - t_{Al})^3 \left( \frac{1 - (\lambda_{Al}/\lambda_{HTPB})}{(\lambda_{blend}/\lambda_{HTPB}) - (\lambda_{Al}/\lambda_{HTPB})} \right)^3 (\lambda_{blend}/\lambda_{HTPB}) \quad (96)$$

where blend identifies the fuel-aluminum mix in the solid. Likewise, in the gas phase, the thermal conductivity is evaluated from homogenization formulae, which are formally identical to those in the solid phase, equation (96), and require knowledge of the gas and particulate thermal conductivities and gas phase volume fractions.

The presence of aluminum in the gas phase is modeled by defining a set of continuous Eulerian fields that describe the particle transport as a sub-scale phenomenon of the gas phase micron-scale processes: those based upon morphological length scales.

The aluminum in the gas phase is present either as liquid aluminum or solid/liquid aluminum oxide. These two states are connected along the global chemical path,



where OX typifies oxidizing species in the product stream and  $m$  is equal to  $3/2$  divided by the number of oxygen atoms in OX. The aluminum reacts with the hot oxidizing species away from the surface because of the inhibiting effect of the oxide shell. Therefore, OX includes the oxygen rich species in the equilibrium gas products of the AP-HTPB combustion. If we assume the specific heat of reactants and products equal, the heat release can be found based upon the heat of formation of the species. Hence, if  $OX = O_2$  in equation (97), the associated heat release is  $Q_{Al} = 7165 \text{ cal/g}$ , while if  $OX = H_2O$  the heat release is  $Q_{Al} = 3957 \text{ cal/g}$ ; note that this value is per gram of aluminum and that the aluminum oxide is assumed in the liquid state. Based upon equilibrium

chemistry calculation, by matching flame temperatures for a AP-HTPB-Al homogenized blend, we select the value to be closer to the latter, and we set  $Q_{Al} = 4500 \text{ cal/g}$ .

Given that the fields are modeled as Eulerian fields, we introduce at this point the concept of Eulerian density of the nano-scale condensed phases, and distinguish it from the Lagrangian density, which is constant and equal to the material value. The Eulerian density is defined as the ratio of the mass of condensed matter to the extension of the volume that contains it, when the volume is taken smaller than all the relevant physical scales. The Eulerian densities,  $\tilde{\rho}_{Al}$ ,  $\tilde{\rho}_{oxide}$  are related to the Lagrangian counterparts,  $\rho_{Al,oxide}$  by,

$$\tilde{\rho}_{Al,oxide} = \rho_{Al,oxide} t_{Al,oxide}, \quad (98)$$

where  $t_{Al,oxide}$  are the volume fractions of aluminum and aluminum oxide, respectively, in the gas phase. Also we note that the overall density is,

$$\rho = \tilde{\rho}_{oxide} + \tilde{\rho}_{Al} + \rho_{gas}, \quad (99)$$

where the density of the gas is found from the Dalton's Law for a mixture of perfect gases,

$$\rho_{gas} = \frac{P}{RT} (1 - t_{Al} - t_{oxide}). \quad (100)$$

Finally, the mass fractions of the dispersed particle phase are,

$$Y_{Al,oxide} = \frac{\tilde{\rho}_{Al,oxide}}{\rho}. \quad (101)$$

The preceding formulas yield a modified thermal equation of state in which the mass fractions of the particulate field modulate the pure gas equation. Specifically, in terms of the Lagrangian densities of the particulate, its mass fractions, the chamber pressure and the temperature,

$$\rho = \frac{p}{RT} \left( 1 + Y_{Al} \left( \frac{p}{RT\rho_{Al}} - 1 \right) + Y_{oxide} \left( \frac{p}{RT\rho_{oxide}} - 1 \right) \right)^{-1}. \quad (102)$$

The transport equations for the Eulerian fields are

$$\rho \frac{DY_{Al,oxide}}{Dt} = \nabla \cdot (\mathcal{D}_{Al,oxide} \nabla Y_{Al,oxide}) + \dot{\omega}_{Al,oxide}, \quad (103)$$

where  $\mathcal{D}$  is a diffusion coefficient which models the motion of the particles with respect to the gas flow due to concentration gradients, a phenomenon necessary to maintain spatial continuity of the concentration fields. Its value is assumed to be very small, and taken to be the fifteenth part of the diffusion coefficient of the gaseous species. This is a convenient value because it corresponds to the minimum value necessary to obtain convergence of the Multigrid Poisson solver for the radiative heat equation. Simulations have demonstrated, however, insensitivity to this parameter and therefore it has not been selected for a parametric study. The term  $\dot{\omega}$  in equation (103) represents the mass conversion of aluminum to alumina and is determined from the aluminum burning model discussed in detail in the following section. Note that, once the mass fractions are calculated, the diameter of the particles is evaluated as,

$$D_{Al} = D_o \left( \frac{Y_{Al}\beta_M}{Y_{Al}\beta_M + Y_{oxide}} \right)^{1/3} \quad (104a)$$



$$D_{\text{oxide}} = D_o \left( \frac{Y_{\text{oxide}}}{Y_{\text{Al}}\beta_M + Y_{\text{oxide}}\beta_\rho} \frac{\beta_M}{\beta_\rho} \right)^{1/3}, \quad (104b)$$

where  $\beta_\rho = \rho_{\text{oxide}}/\rho_{\text{Al}}$ , while  $\beta_M = M_{\text{oxide}}/(2M_{\text{Al}})$ , with  $M$  the molecular weight.  $D_o$  is the initial diameter of the particles as they are ejected from the surface.

### 3.5 Aluminum Burning

#### 3.5.1 Model

The burning of aluminum spheres is modeled using a power law representation of the volume consumption of the particles in a constant property environment,

$$\sigma_v := \frac{1}{V} \frac{dV}{dt} = -k_v D_{\text{Al}}^{-n}, \quad (105)$$

where the exponent  $n$  is commonly assumed to be close to 2 and the cofactor,  $k_v$ , is dependent on the local conditions, such as temperature, pressure and oxidizing species concentration. The exponent and cofactor can be obtained from experimentally measured particle burn out times if the surrounding conditions are assumed invariant of time. Experimental correlations are usually presented as

$$t_{\text{burnout}} = k_b D_o^{n_d} T^{-n_t} P^{-n_p} \chi_{\text{ox}}^{-n_o} \mathcal{D}_{\text{rel}}^{-1}, \quad (106)$$

where  $\chi_{\text{ox}}$  is the concentration of oxidizing species active along the path equation (97) and  $\mathcal{D}_{\text{rel}}$  is a diffusion parameter, see the discussion in Najjar *et al.* [23] for more details. Time integrating between the initial time and the burn-out time yields the relations,

$$n = n_d \quad (107)$$

$$k_v = \frac{3}{k_b n} T^{n_t} P^{n_p} \chi_{\text{ox}}^{n_o} \mathcal{D}_{\text{rel}}. \quad (108)$$

The value of  $k_b$  obtained by different experimental procedures can differ by several orders of magnitude. No power law exists that is valid in all the range of aluminum diameters of interest to solid propellant analysis.

Another modeling uncertainty is rooted in the fact that aluminum near the surface burns differently before and after the oxide shell break-up. For micron-scale particles, the shell break-up is commonly identified with the melt temperature of the aluminum oxide,  $T_{\text{melt,oxide}} = 2350\text{K}$ ; for nano-scale particles the formation and re-sealing of cracks makes this definition more ambiguous. Below such transitional temperature the micron-scale aluminum is assumed to undergo negligible oxidation. On the contrary, nano-scale particles are considered to undergo significant oxidation at temperature below that of the shell break-up, at approximately the aluminum melting temperature [24,25]. Experiments by Bazyn *et al.* [26], have shown that the burn-out time of nano-scale particles is essentially temperature insensitive for ambient value lower than approximately 2000 K, while it sharply decreases of an order in magnitude above such a temperature, demonstrating the presence of two stages of the burning in nano-scale aluminum. The first stage, for  $T < T_{\text{melt,oxide}}$ , is characterized as the core shrinking phase of the burning, a strictly diffusion limited and temperature independent process, Aita *et al.* [27]; the reason why the core shrinking phase is not important at the micron-scale level is the larger volume/surface ratio of the particles. The second stage, valid

after the oxide shell brakes, is more complex and its model should take into account aluminum kinetics paths.

Widener and Beckstead [28] model offers the best available correlation for the full combustion stage of aluminum burning. This correlation was obtained for micron-size aluminum so it does not necessarily extend to the nano-scale range. By using Widener and Beckstead correlation we set,  $k_b = 1138$ ,  $n_t = 1.57$ ,  $n_p = 0.2$ ,  $n_o = 0.39$ , when the dimensions are taken to be degree Kelvin, atmosphere and microns. Due to the significant disparity in the burn-out times between the two stages of burning, the core shrinking stage is disregarded, by effectively setting  $k_v = 0$  when the temperature is lower than the melting temperature of the oxide.

Experiments by Bazyn *et al.* [26] have shown that the temperature overshoot above ambient of aluminum particle in constant ambient experiments is limited by the dissociation of alumina. To reproduce this phenomenon, aluminum burning is turned off when the gas temperature reaches the boiling point of the  $\text{Al}_2\text{O}_3$ . The average value for the aluminum oxide boiling point in the pressure range  $P \in 20\text{-}70$  atm is taken to be  $T_{\text{boil,oxide}} = 4100\text{K}$ . These considerations yield a transformed particle burning law,

$$\sigma_v = \begin{cases} -k_v D_{\text{Al}}^{-n} & T_{\text{melt,oxide}} < T < T_{\text{boil,oxide}} \\ 0 & T < T_{\text{melt,oxide}}, T > T_{\text{boil,oxide}} \end{cases} \quad (109)$$

Equation (109) is then used to evaluate the source terms in (103), resulting in the formalisms,

$$\dot{\omega}_{\text{Al}} = \rho Y_{\text{Al}} \sigma_v \quad (110a)$$

$$\dot{\omega}_{\text{oxide}} = -\dot{\omega}_{\text{Al}} \beta_M. \quad (110b)$$

### 3.5.2 Uncertainty and parametric study

Due to the high degree of uncertainty in the burning formulas, a parametric study will be conducted by pre-multiplying  $k_v$  by a factor, denoted in the following as  $\phi_v$ ,

$$k_v = \frac{3\phi_v}{k_b n} T^{n_t} P^{n_p} \chi_{\text{ox}}^{n_o} \mathcal{D}_{\text{rel}}. \quad (111)$$

The factor will be varied by effectively calibrating the model versus experimental data. The calibration shows  $\phi_v$  to be always less than one in order to obtain sensible results, demonstrating that micro-scale burn rate correlations over-predicts the burn rate of nano-scale particles.

## 4 Results

### 4.1 Validation Study

For validation we consider propellant P01a of [2]. The formulation for this propellant is 15% by weight nano-aluminum, 17% HTPB binder, and 68% AP. The AP is bimodal with 80% by weight 150 micron AP and 20% 75 micron AP. The morphology is modeled using *Rocpack*, our proprietary packing code. A 3,124 particle pack that models P01a is shown in Figure (1). Figure (2) shows a grid resolution study for three different grids. What is plotted is the surface-averaged burn rate as a function of distance burned, and for three different grids. Note that the surface-averaged burn rates

are not constant due to morphology burn-through. We comment here that the grid is stretched in the nominal  $y$ -direction, so only 60 grid points are needed to adequately resolve the combustion dynamics as well as the far field conditions. The grids in the  $(x, z)$ -directions are uniform. The burn rates for the three grids are: 0.9097 ( $40 \times 40 \times 60$ ); 0.9649 ( $80 \times 80 \times 60$ ); 1.0152 ( $160 \times 160 \times 60$ ). It is seen that the middle grid gives adequate resolution to within 5%, and so we use this grid in all subsequent simulations. Figure (3) shows the surface-averaged burn rate as a function of distance burnt for various values of the uncertainty parameter  $\phi_v$  and for a pressure of 20 atm. The burn rates are: 0.8568 cm/s ( $\phi_v = 0.15$ ), 0.8305 cm/s ( $\phi_v = 0.08$ ), 0.8137 cm/s ( $\phi_v = 0.06$ ), 0.7796 cm/s ( $\phi_v = 0.04$ ). The value for  $\phi_v = 0.04$  is reasonable close to the value reported in [2], and so we fix this parameter and use it in all subsequent simulations.

Figure (4) plots the surface-averaged burn rate as a function of distance burnt and for different pressures. Note that the surface-averaged burn rates are not constant due to morphology burn-through. Figure (5) compares the burn rate from the simulations to those of the experimental data of [2]. For both the simulations and the experiments we also show the error bars. Note the overall good agreement between simulations and experiments. Figures (6-8) plots the surface temperature and the radiative transport,  $-\nabla \cdot \mathbf{q}_r$ , for three different times, respectively.

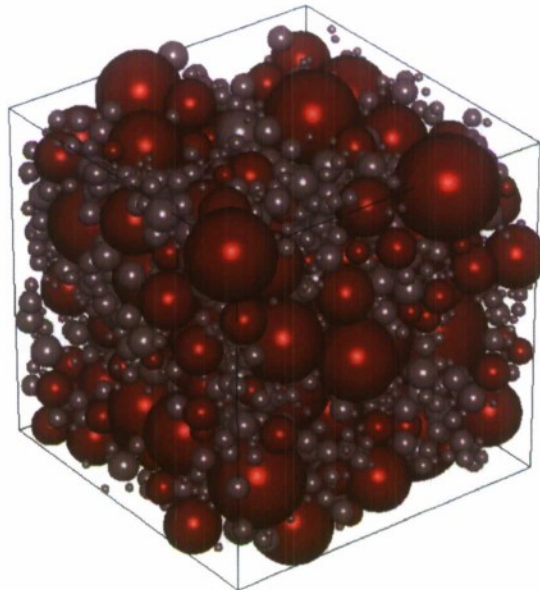


Figure 1: A 3,124 particle pack that models P01a of [2]. The coarse AP particle distribution is shown in red, and the fine AP particle distribution is shown in gray. The void space is the blend, a homogeneous mixture of very fine AP, binder, and nano-aluminum particles. The domain is periodic, and only those spheres inside the cube are plotted. The cube dimension is  $1079.79 \times 1079.79 \times 1079.79 \mu\text{m}^3$ .

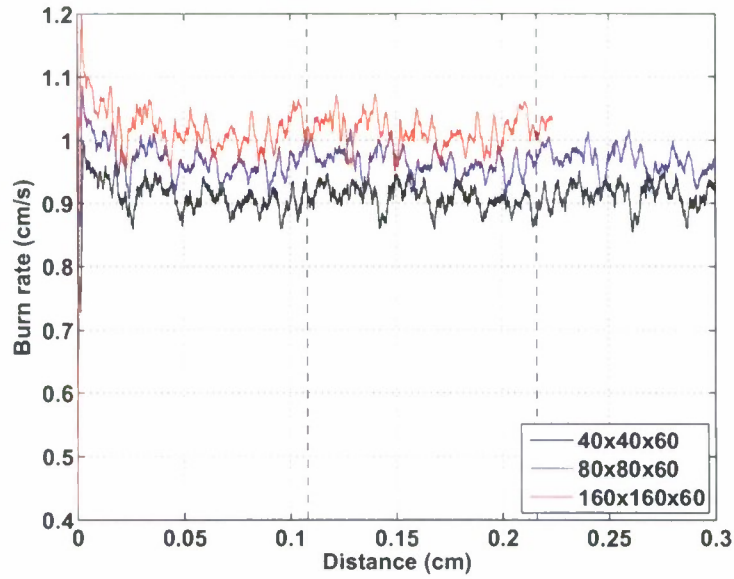


Figure 2: Grid resolution study showing surface averaged burn rates as a function of distance burnt at a pressure of 40 atm and with  $\phi_v = 0.04$ . The average burn rates for the three grids are: 0.9097 ( $40 \times 40 \times 60$ ); 0.9649 ( $80 \times 80 \times 60$ ); 1.0152 ( $160 \times 160 \times 60$ ). In each case the simulations were run on 40 processors. The dash lines correspond to the length of the periodic pack. Pack shown in Figure (1).



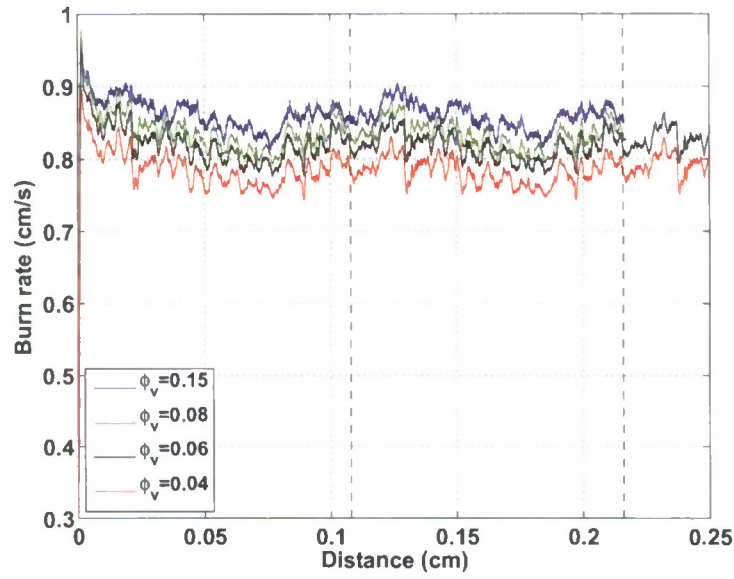


Figure 3: Surface-averaged burn rate as a function of distance burnt for various values of  $\phi_v$  and at a pressure of 20 atm. The average burn rates are: 0.8568 cm/s ( $\phi_v = 0.15$ ), 0.8305 cm/s ( $\phi_v = 0.08$ ), 0.8137 cm/s ( $\phi_v = 0.06$ ), 0.7796 cm/s ( $\phi_v = 0.04$ ). The dash lines correspond to the length of the periodic pack.

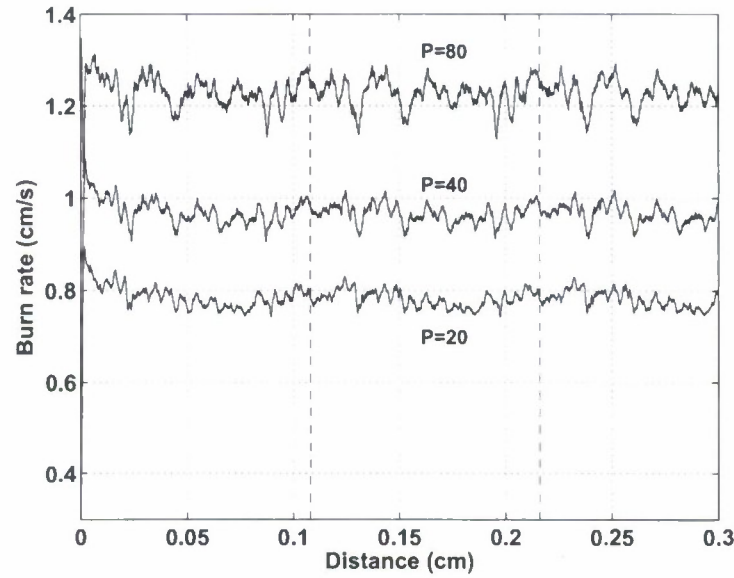


Figure 4: Surface-averaged burn rate as a function of distance burnt for various pressures (20, 40 and 80 atm) and for  $\phi_v = 0.04$ . The average burn rates are 0.7796 cm/s (20 atm), 0.9649 cm/s (40 atm), and 1.2256 cm/s (80 atm). The dash lines correspond to the length of the periodic pack.

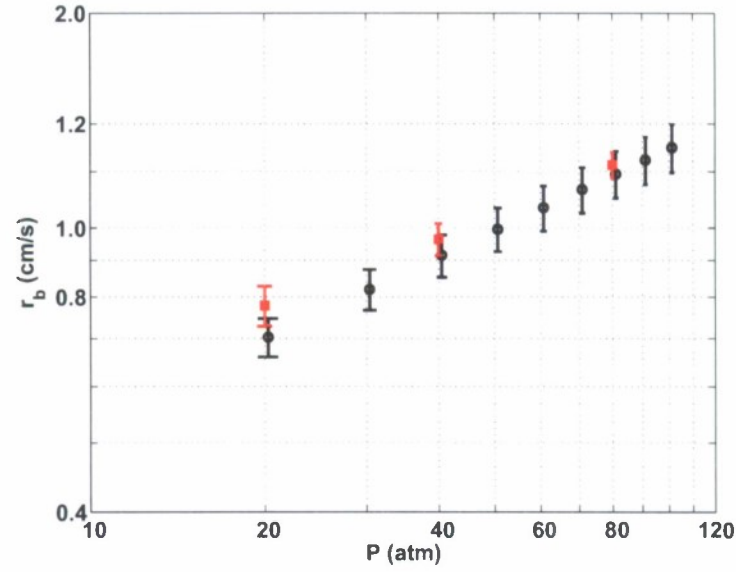


Figure 5: Burn rate as a function of pressure for  $\phi_v = 0.04$ . Numerical values are shown as red boxes with 5% error bars. Also shown are the experimental values from [2], shown as black circles with experimental error bars.

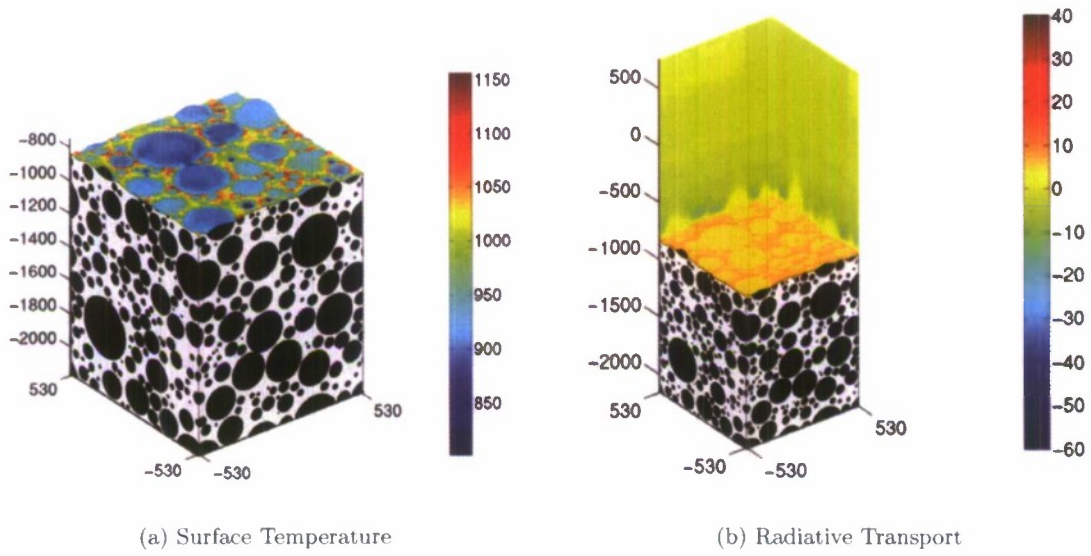


Figure 6: Plot of surface temperature and radiative transport at time 0.090964 s.

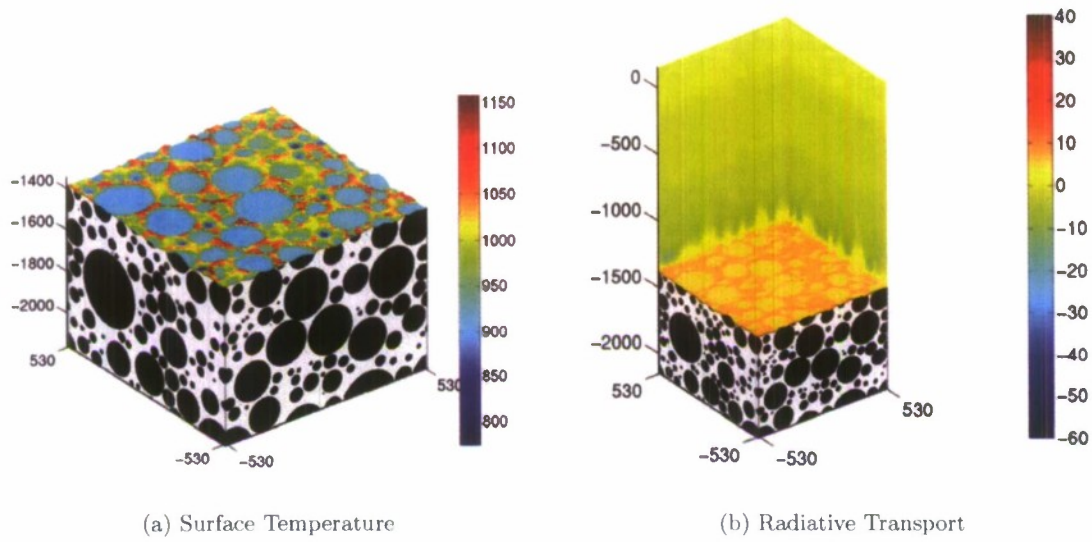


Figure 7: Plot of surface temperature and radiative transport at time 0.15296 s.

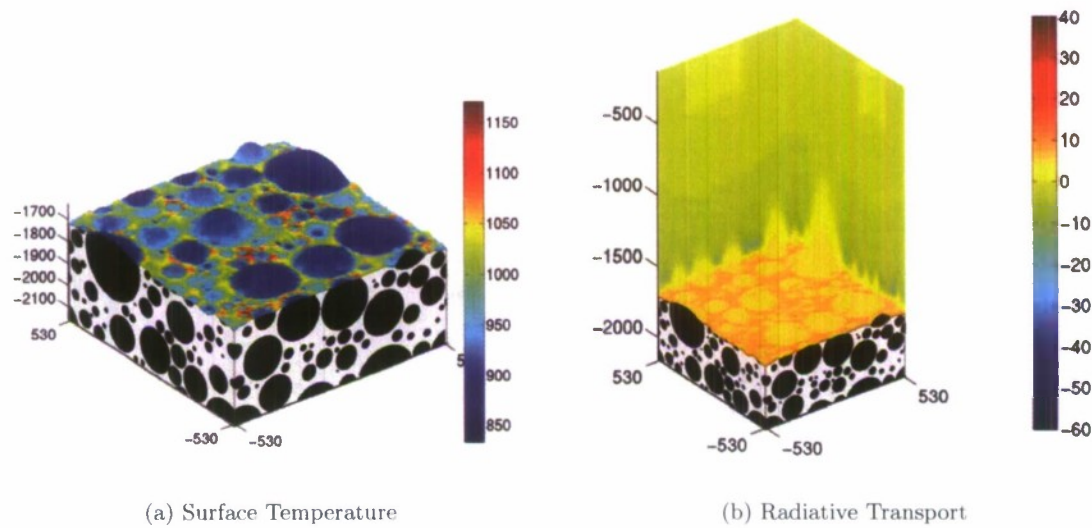


Figure 8: Plot of surface temperature and radiative transport at time 0.18596 s.

## 4.2 Purdue Propellants

In a preliminary study, propellants containing AP and nano-aluminum were mixed at the mixing facility at Purdue University. The propellant mixer is shown in Figure (9). The baseline batch, which we will call series A, is based on historic Purdue formulations of micron-aluminum loaded AP/HTPB composites 13 with a direct substitution of nano-aluminum for the micrometric aluminum. The nano-aluminum used was Novacentrix 80nm aluminum powder (it should be noted that the size distribution for this specific batch is outside of manufacturer specified tolerances), and all other materials were from Firefox Enterprises, a pyrotechnic supply for amateur hobbyists. Table 4 lists the mix formulation.

Table 4: Series A Propellant Formulation

Ingredient	Function	Percent Weight
Hydroxyl-terminated Polybutadiene (R-45M)	Binder and Fuel	14.84
Ammonium Perchlorate (60-130 $\mu$ m Diameter)	Oxidizer	38.64
Ammonium Perchlorate (200 $\mu$ m Diameter)	Oxidizer	25.00
2 Ethyl Hexyl Acetate	Plasticizer	4.58
Isonate 143-L - Modified MDI	Curing Agent	2.95
HX-878 - Tepanol	Bonding Agent/Curative	0.60
Lecithin	Processing Aid	0.50
Polydimethylsiloxane	Anti-Foam Agent	2 drops

To determine the effect of nano-aluminum loading, we construct three propellants with the same coarse-to-fine (C/F) ratio of AP as the baseline batch, but vary the weight of nano-aluminum from 6%, 12%, and 18%. Table 5 shows the percent weight of the various ingredients used in the simulation matrix. Representative packs of 2,000 particles are shown in Figure (10). The length of each side of the cubes are given in Table 5. The surface-averaged burn rate as a function of distance burnt is shown in Figure (11). Note that the surface-averaged burn rates are not constant due to morphology burn-through. The burn rate for the lowest aluminum content, Figure (11a), has larger variations about the mean than the other two formulations, which indicates a more erratic burning behavior. The corresponding burn rates are shown in Figure (12), at a pressure of 68 atm. The black squares correspond to the simulations for the three propellant formulations A1, A2 and A3, and the blue circle corresponds to the experiments carried out at Purdue for propellant mix A2. The 95% confidence level is also shown in blue. The burn rate values from the simulations are 1.0725 cm/s (A1; 6%), 1.1439 cm/s (A2; 12%), and 1.0902 cm/s (A3; 18%). Note that the largest value of the burn rate corresponds to 12% nano-aluminum. The experimental burn rate for propellant A2 (shown as the blue circle) is 1.26 cm/s (see discussion below). This corresponds to a 10% difference between the simulation and the experimental burn rate; considering the error bars are probably about 5% for both the experiments and the simulations, this represents an excellent result.

Due to the small amount of propellant needed, samples were prepared by hand-mixing the chemicals in a plastic bag as opposed to the Ross mixer. Despite concerns about adequate rheology and particle dispersion, this procedure has been shown to provide inconsequential differences 6. Propellants were also cast in an oven at 140°F for a minimum of two days, and cast in either



Mix	nano-Al	HTPB	Coarse AP	Fine AP	$L$ ( $\mu\text{m}$ )
A1	6	23.47	27.734	42.796	1204.5
A2	12	23.47	25.374	39.156	1235.2
A3	18	23.47	23.015	35.515	1270.2

Table 5: Simulation matrix varying percent weight of nano-aluminum with fixed C/F AP ratio of 0.6480331. The last column corresponds to the length of one side of a periodic cube using 2,000 total particles.

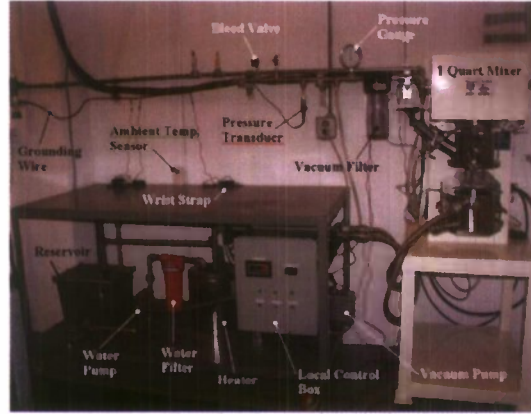


Figure 9: Propellant mixer at Purdue University.

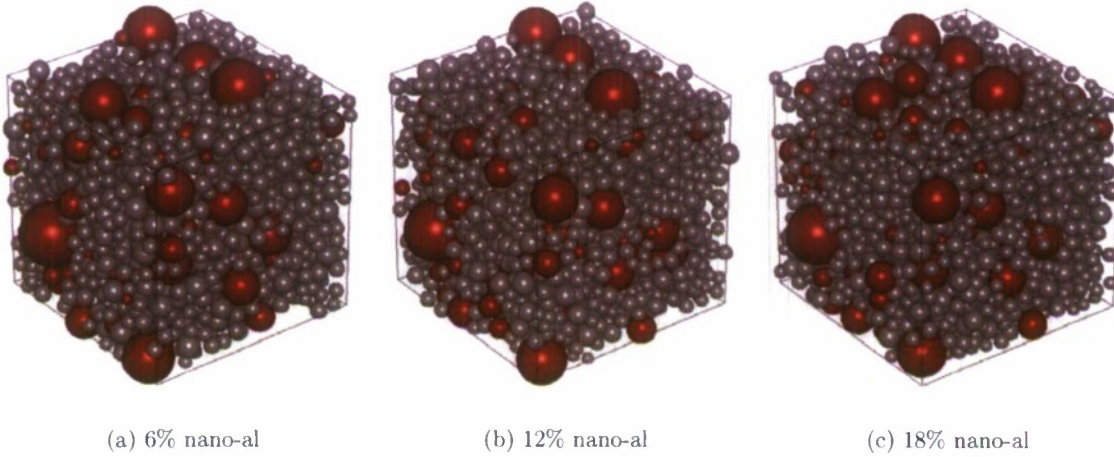


Figure 10: Particle packs that model Series A from Purdue. The coarse AP particle distribution is shown in red, and the fine AP particle distribution is shown in gray. The void space is the blend, a homogeneous mixture of very fine AP, binder, and nano-aluminum particles. The domain is periodic, and only those spheres inside the cube are plotted.

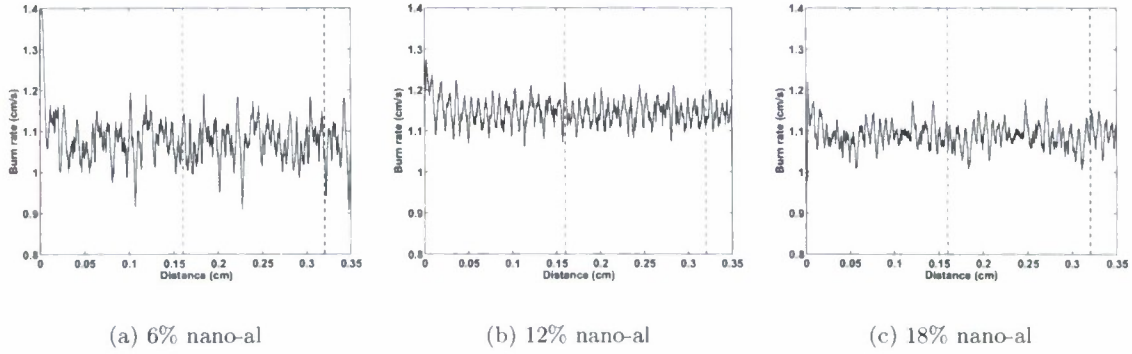


Figure 11: Surface-averaged burn rates as a function of distance burnt at a pressure of 68 atm.

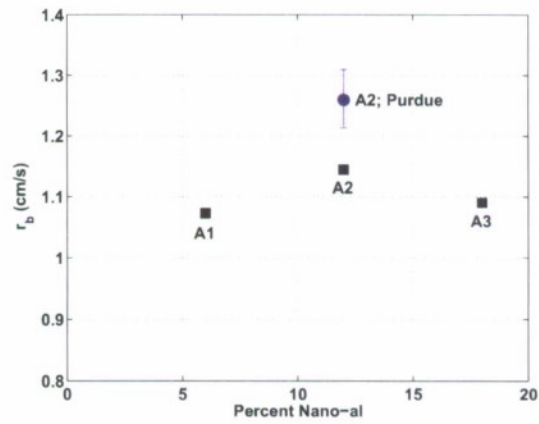


Figure 12: Burn rate as a function of percent nano-aluminum. Pressure is 68 atm. The black squares correspond to the simulations, and the blue circle corresponds to the experiments carried out at Purdue. The 95% confidence level is also shown in blue.



Figure 13: Propellant cast in quartz tubes.



Figure 14: Propellant cut from cast block.

quartz tubes or as a solid block and cut into individual strands, as shown in Figures (13) and (14), respectively.

Furthermore the cut strands are inhibited by either using a polyurethane or epoxy coating so that the propellant can only burn on one surface. Figure (15) shows a fully prepared propellant strand ready to go into the 6000 psi Crawford bomb.

Initial burns with the A1, A2, and A3 mixes cast in quartz tubes yielded uneven, non-planar burns due to poor packing and air pockets within the sample, illustrated in Figure (16). Consequently, burn rate analysis is erratic and inconsistent.

A redo of mix A2, cast as a block and inhibited with epoxy, resulted in much more planar burns, shown in Figure (17), and allows for consistent surface tracking using the open source program Tracker [33]. Analysis of four strands burned at an initial temperature of 60.7°F and initial pressure of 68 atm resulted in a burn rate of 1.26 cm/s.



Figure 15: Inhibited propellant prepped to go into Crawford bomb. Shown also is NiChrome ignition wire.

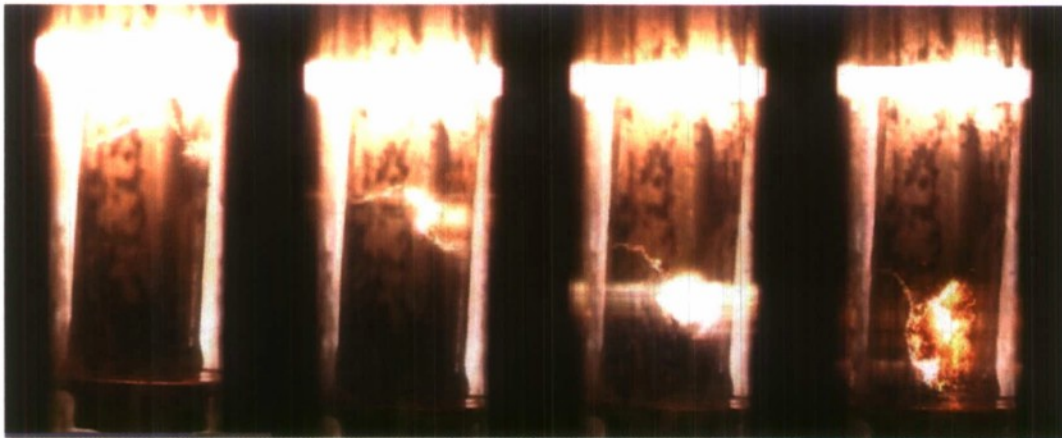


Figure 16: Video images from an uneven, nonplanar burn.



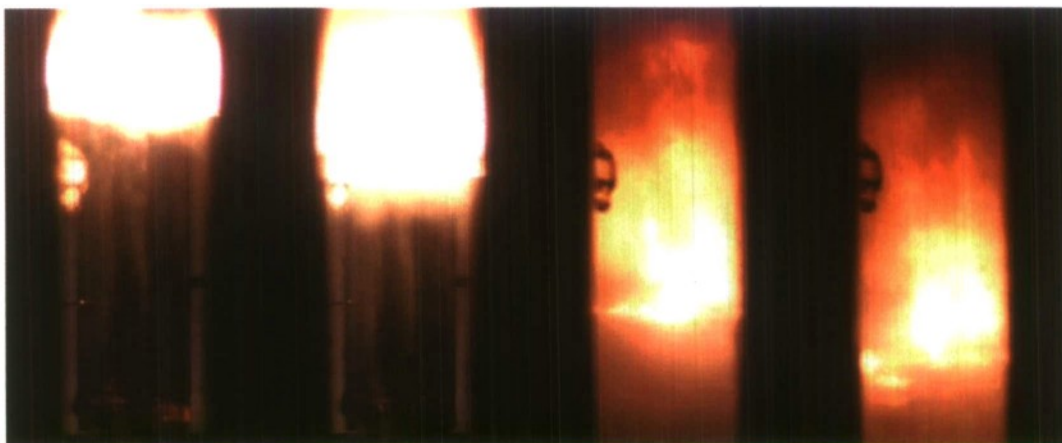


Figure 17: Video images from an even, planar burn.

## 5 Purdue Experimental Results

In efforts to firmly validate the simulation codes developed by IllinoisRocstar LLC, a test matrix of propellants has been developed at Purdue facilities for computer model verification. The following sections detail the characterization of these propellants, the experimental approach to meet the technical objectives for this project, and the current results of work done.

### 5.1 Propellant Characterization

For the simulation codes to accurately model a given propellant, information must be known about its composition and particle size distributions of relevant constituents. Since propellant mass composition is easily controlled, a simple test matrix of propellants was established to provide validation and calibration for the IllinoisRocstar code. The first set of propellants, designated Series A, consists of nano-aluminum (nAl) fuel, fine ammonium perchlorate (fAP) oxidizer, coarse ammonium perchlorate (cAP) oxidizer, hydroxyl-terminated polybutadiene (HTPB) binder, and various other mixing and curing additives. With the exception of the 80nm nano-aluminum, all Series A ingredients are purchased from Firefox Enterprises, a commercial hobby rocketry and fireworks supplier. Ethyl hexyl acetate (EHA), polydimethylsiloxane (PDMS), and lecithin are all used during the mixing process to allow for easier mixing, and isonate 143L and HX-878 (tepanol) are used for curing. A summary of the ingredients is shown in Table 6.

For a preliminary test of the simulation code over a range of compositions, the solids composition was varied over three formulations. Based on historical Purdue propellants, the total solids composition, coarse to fine ratio of AP (cAP/fAP), and binder composition were held constant at a nominal 76.53%, 0.648, and 23.47%, respectively. Within the solids content, the AP percent composition decreased as needed while the nano-aluminum loading increased from nominal values of 6%, 12%, and 18%. A summary of the actual solids and binder composition are listed in Tables 7 and 8, respectively.

For Series A propellants, 80nm, uncoated nano-aluminum powder from NovaCentrix was chosen for its readily available supply at Purdue University. In order to determine its particle size distri-

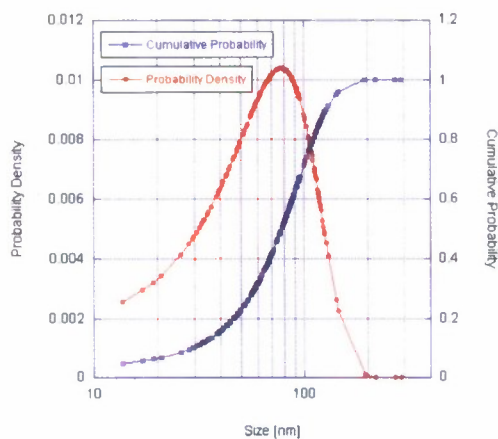
bution, SEM or TEM imaging is needed. For these mixes specific imaging is not available for the specific nano-aluminum inventory T2R0-24-3, but by argument of similarity the powder is assumed to be the same as two other NovaCentrix 80nm, uncoated powder inventory lots. Based on SEM imaging, shown in Fig. 18, and manual analysis, size distribution of nano-aluminum powders can be defined using probability density and cumulative probability. Plots are presented in Figs. 19(a) and 19(b) for lots M2665B\_6410 and M2666\_5406, respectively, and summarized in Table 9.



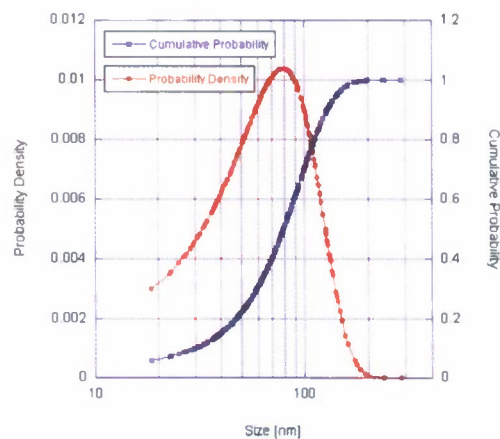
Figure 18: SEM Imaging of NovaCentrix 80nm Nano-Aluminum, Lot M2666\_5406

Table 6: Series A Propellant Constituents

Ingredient	Function	Source
80nm Nano-Aluminum	Fuel	NovaCentrix
Ammonium Perchlorate (60-130 $\mu$ m Diameter)	Oxidizer	Firefox Enterprises
Ammonium Perchlorate (200 $\mu$ m Diameter)	Oxidizer	Firefox Enterprises
Hydroxyl-Terminated Polybutadiene (HTPB)	Binder/Fuel	Firefox Enterprises
2 Ethyl Hexyl Acetate (EHA)	Plasticizer	Firefox Enterprises
Lecithin	Processing Aid	Firefox Enterprises
Polydimethylsiloxane (PDMS)	Anti-foam Agent	Firefox Enterprises
Isonate 143L - Modified MDI	Curing Agent	Firefox Enterprises
HX-878 (Tepanol)	Bonding Agent/Curative	Firefox Enterprises



(a) Lot M2665B\_6410



(b) Lot M2666\_5406

Figure 19: NovaCentrix 80nm Nano-Aluminum Size Distribution

Table 7: Series A Solids Composition

Formulation	%Nano-Aluminum	%Coarse AP	%Fine AP	cAP/fAP Ratio	Total
A1	6.00	27.72	42.81	0.648	76.53
A2	12.03	25.43	39.22	0.648	76.68
A3	18.00	23.00	35.50	0.648	76.50

Table 8: Series A Binder Composition

Formulation	%HTPB	%EHA	%Lecithin	%PDMS	%Isonate 143L	%Tepanol	Total
A1	14.84	4.58	0.50	Negligible	2.95	0.60	23.46
A2	14.84	4.59	0.50	Negligible	2.96	0.60	23.32
A3	14.83	4.58	0.51	Negligible	2.94	0.65	23.50

Table 9: NovaCentrix 80nm Nano-Aluminum Size Distribution

Inventory Lot	Mean Size [nm]	Standard Deviation [nm]
M2665B_6410	77.90	38.38
M2666_5406	79.14	38.43
Average	78.52	38.41

For larger micrometric-size powders such as the coarse and fine ammonium perchlorate, size distribution can be determined using a Sympatec helium-neon laser optical system (HELOS), shown in Fig. 20, and WINDOX 4 data analysis software. With this setup dry AP powder is dusted in front of a laser source and the resulting diffraction pattern is captured by an R3 or R6 Fourier lens whose nominal measurement ranges are 0.5 - 175 $\mu\text{m}$  and 9-1750 $\mu\text{m}$ , respectively. From prior work with the R3 lens, all AP powders are composed of a very small amount of particles less than 10 $\mu\text{m}$  in diameter, and consequently data primarily comes from the R6 lens unless otherwise noted. Figs. 21(a) - 21(b) and 22(a) - 22(b) plot the probability density and cumulative probability of Firefox AP crystals; the mean and standard deviation are summarized in Table 10.



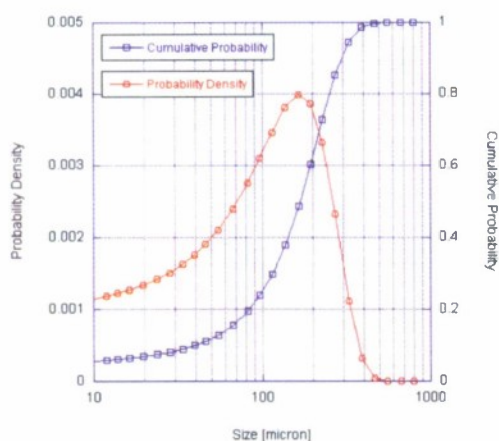
Figure 20: Sympatec HELOS Particle Sizer

Table 10: Series A Ammonium Perchlorate Size Distribution

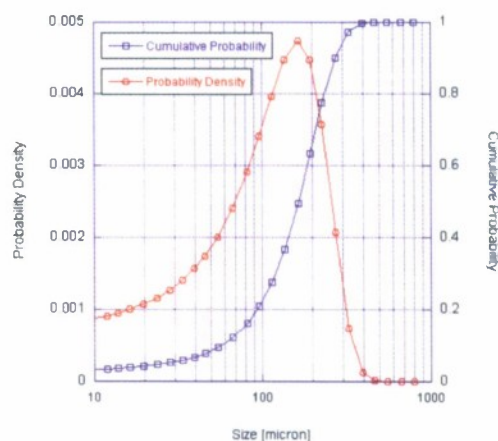
Reference Name	Sample	Mean Size [ $\mu\text{m}$ ]	Standard Deviation [ $\mu\text{m}$ ]
Firefox 60-130 $\mu\text{m}$	Sample 1	167.76	99.89
	Sample 2	165.03	84.10
	Average	166.40	92.00
Firefox 200 $\mu\text{m}$	Sample 1	217.45	79.41
	Sample 2	206.11	75.46
	Average	211.78	77.44

With a baseline propellant matrix established for steady-state tests, the next series of propellants, Series B, focused on using higher quality ingredients for more consistent results for dynamic analysis. For the first composition, propellant B1, the percent composition is based on Galfetti



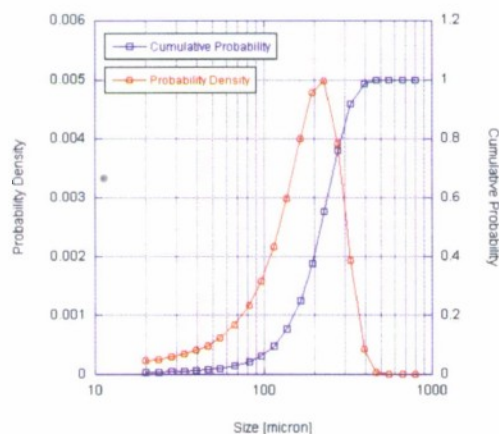


(a) Sample 1

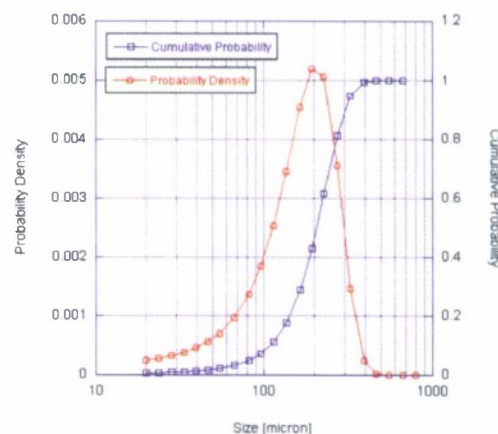


(b) Sample 2

Figure 21: Firefox 60-130 $\mu$ m Ammonium Perchlorate Size Distribution



(a) Sample 1

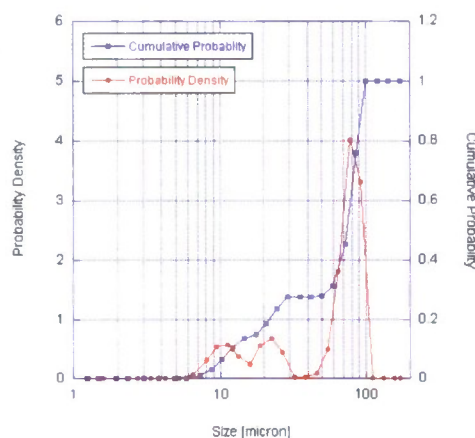


(b) Sample 2

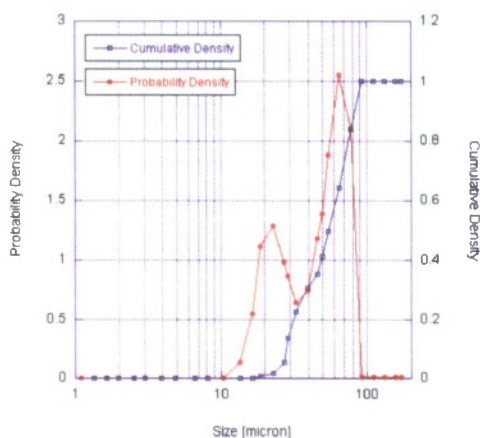
Figure 22: Firefox 200 $\mu$ m Ammonium Perchlorate Size Distribution

et al's baseline formulation [2] using newly acquired NovaCentrix 80nm nano-aluminum and 20 $\mu$ m and 200 $\mu$ m AP from Alliant Techsystems Inc (ATK). Since SEM imaging is not yet available for the new stock of 80nm nano-aluminum, the size distribution is again assumed to be the same as the data listed in Table 9 since they are expected to be very similar to other 80nm powders. The AP size distribution is available from the HELOS particle sizer, shown in Figs. 23(a) - 23(b) and 24(a) - 24(b), where the R3 Fourier lens is used for the 20 $\mu$ m powder due to its nominally smaller size. The multiple peaks in Figs. 23(a) and 23(b) are due to moisture exposure during sample transportation

which results in noticeable clumping. Consequently, further analysis is needed before calculating the statistical mean and standard deviation of the 20 $\mu$ m AP.

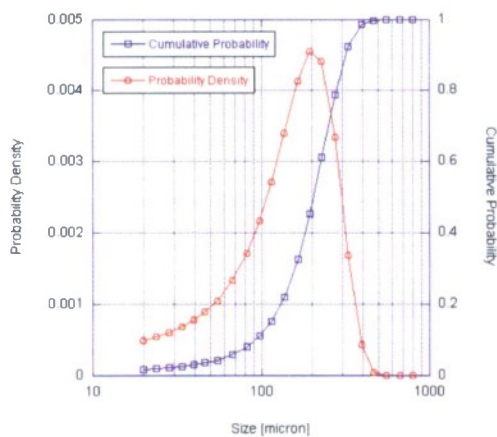


(a) Sample 1

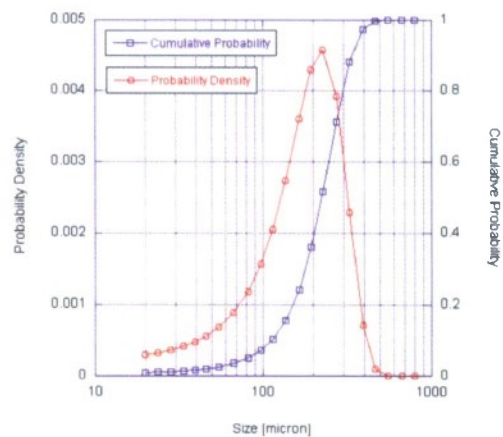


(b) Sample 2

Figure 23: ATK 20 $\mu$ m Ammonium Perchlorate Size Distribution



(a) Sample 1



(b) Sample 2

Figure 24: ATK 200 $\mu$ m Ammonium Perchlorate Size Distribution

For comparison, the HELOS particle size data is compared to manufacturer provided specifications generated either by sieve based measurements (Rotap) for the 200 $\mu\text{m}$  AP or air classifying mill (ACM) for the 20 $\mu\text{m}$  AP. Shown in Figs. 25(a) and 25(b), qualitative analysis suggests that the HELOS consistently overestimates the mean particle size by a small amount; the general shape of the HELOS curve shows no correlation. To determine which measurement method is most correct, photographic imaging and manual analysis of particle sizes is needed. Available statistical information is tabulated in Table 11 and the complete propellant B1 formulation is shown in Tables 12 and 13.

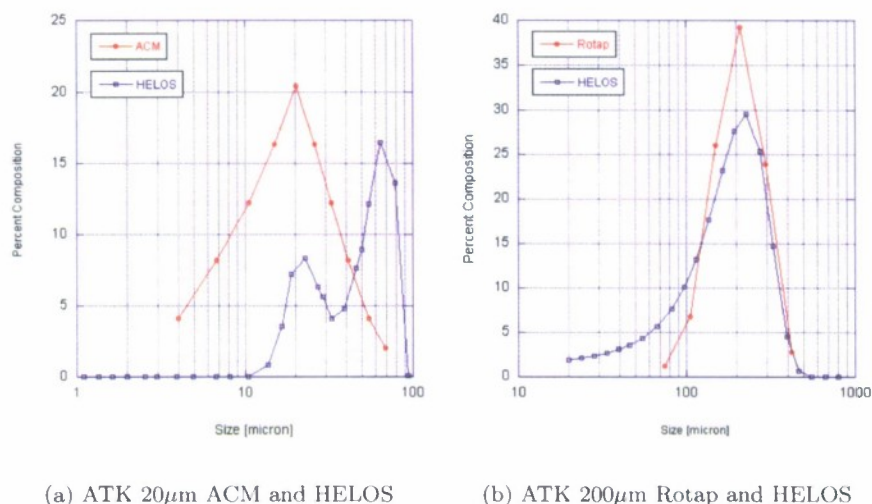


Figure 25: Comparison of Manufacturer and Purdue Particle Size Data

Table 11: Series A Ammonium Perchlorate Size Distribution

Reference Name	Measurement Type	Mean Size [ $\mu\text{m}$ ]	Standard Deviation [ $\mu\text{m}$ ]
ATK 20 $\mu\text{m}$	ACM	20.11	19.92
	HELOS	n/a	n/a
ATK 200 $\mu\text{m}$	Rotap	n/a	n/a
	HELOS	214.29	87.11

Table 12: Series B Solids Composition

Formulation	%Nano-Aluminum	%Coarse AP	%Fine AP	cAP/fAP Ratio	Total
B1	15.00	54.40	13.60	4.00	83.00

## 5.2 Experimental Setup and Results

For Series A propellants, the primary goal was to provide a wide range of steady-state burn rate data for computer model calibration. To accomplish this, propellants were mixed by hand and

Table 13: Series B Binder Composition

Formulation	%HTPB	%EHA	%Lecithin	%PDMS	%Isonate 143L	%Tepanol	Total
B1	10.74	3.31	0.37	Negligible	2.14	0.44	17.00

oven-cured for at least two days. Cast propellant blocks were then cut into 6x6x38mm (0.25 x 0.25 x 1.5 in) strands and inhibited with epoxy on all sides except the top surface to provide for a planar burn. Although a strand heater has been tested operational, initial tests minimize the effects of temperature variation. Room temperature was kept between 15.5°C and 18.3°C (60-65°F) and strands were left in the open at least 30 minutes to come to thermal equilibrium. Strands were then loaded inside a windowed pressure vessel and ignited with nichrome wire at initial pressures of 34, 47.6, 68, 95.2, or 129.3 atmospheres (500, 700, 1000, 1400, and 1900 psia). A camera recorded the burning propellant strand at 30 frames per second and the burn surface progression is manually tagged frame-by-frame using video analysis tool, Tracker [33]. Figs. 26 and 27 demonstrate a typical planar burn and show how Tracker is able to follow the burn surface at each frame throughout the burn.

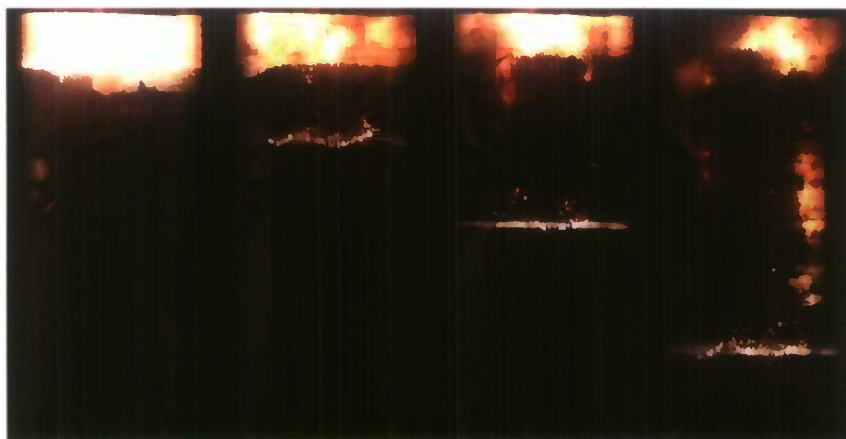


Figure 26: Planar Propellant Burn

The data is then plotted on a log-log graph and fitted to using St. Robert's Law,  $r_b = ap^n$ , where  $r_b$  is the burn rate in cm/s,  $a$  is the burn coefficient,  $p$  is the vessel pressure in atm, and  $n$  is the pressure exponent. Data for Series A propellants is shown in Fig. 28 as well as a comparison burn at 68atm with propellant B1. Series A burn coefficients and pressure exponents are listed in Table 14.

Table 14: Series A Burn Rate Constants

Formulation	Burn Coefficient, $a$	Pressure Exponent, $n$	Curve Fit $R^2$
A1	0.333	0.268	0.858
A2	0.300	0.332	0.910
A3	0.369	0.382	0.491



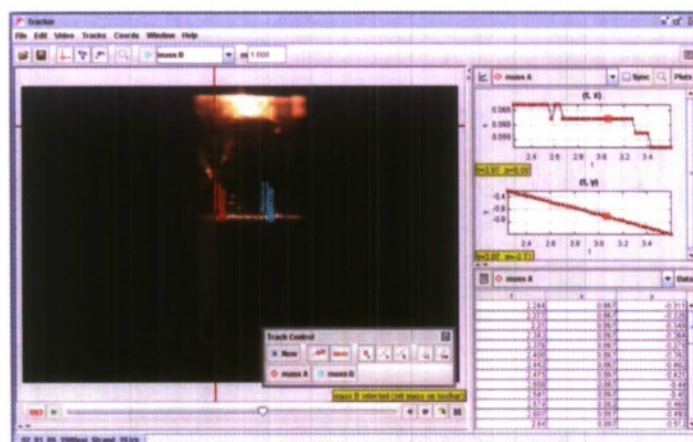


Figure 27: Tracker Video Analysis Software

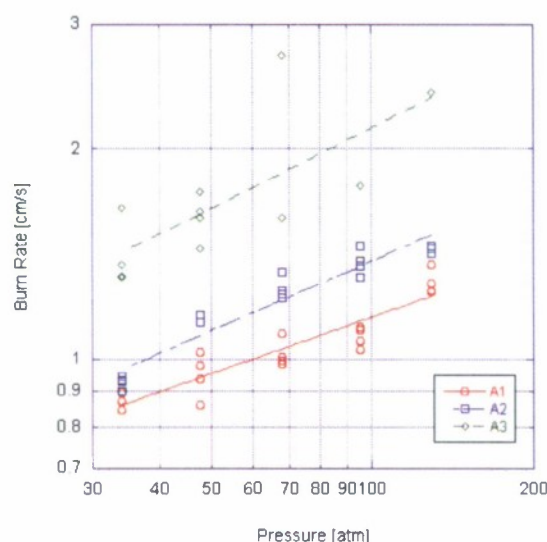


Figure 28: Series A Propellant Burn Rate

Evaluating St. Robert's Law using the coefficients in Table 14 then allows comparison with the theoretical burn rate predicted by the simulation code at 68atm. The result is shown in Table 15. To explain the large discrepancy between theoretical and experimental A3 propellant, in comparison to other Series A strands, A3 showed significantly more air pockets which would consequently result in a higher measured burn rate. Surface scans of propellants A1-A3 as well as propellant B1 are presented in Figs. 29(a) - 29(d) for comparison.

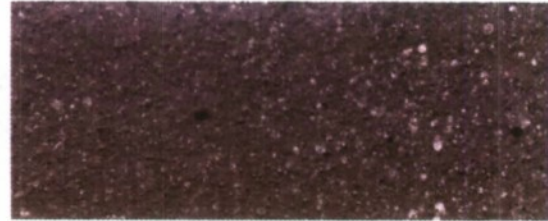
Although Sammet et. al [6] have demonstrated little difference between hand and mechanical mixes, propellant B1 was made using Purdue's Ross vacuum mixer in efforts to maximize the consistency and repeatability of future work. Qualitative analysis of Figs. 29(a) - 29(d) suggests slight improvement in AP crystal dispersion, but markedly minimizes the number of air pockets.

Table 15: Comparison of Theoretical and Experimental Burn Rate

Formulation	Theoretical Burn Rate [cm/s]	Experimental Burn Rate [cm/s]	Percent Difference
A1	1.0725	1.032	1.94
A2	1.1439	1.218	3.12
A3	1.0902	1.849	25.8



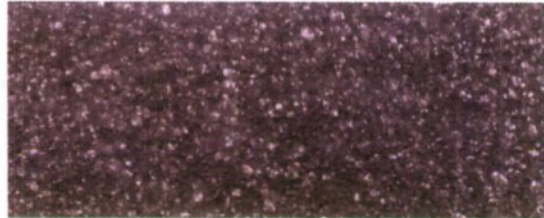
(a) A1



(b) A2



(c) A3



(d) B1

Figure 29: Comparison of Series A and B Propellant Quality

Additionally, unlike previous mixes, further steps were taken to ensure adequate rheology in B1 by ultrasonically dispersing the nano-aluminum powder a hexane solution to reduce agglomeration.

To start the dynamic analysis objective of the program, tests for B1 consisted of cutting propellant blocks into smaller 6x6x6mm cubes (0.25 x 0.25 x 0.25in) and inhibited on all but the top face with a thin layer of polyurethane for better burn surface imaging. The CO<sub>2</sub> laser was aimed and calibrated to output 7.5 watts of power using a Coherent LM-200 laser power detector and the ignition transient was captured with a high-speed Phantom camera recording at 10,000 frames per second. Figs. 30(a) - 30(c) show the ignition for a constant-power laser pulse over the entire burn, and since only few tests were able to be completed before failure of the reflective mirror, no better images were taken.

## 6 Future Work

Due to the very consistent results from this batch, further A-series mixes will continue to use the same hand-mix and casting procedures to provide calibration data over a wide range of operating

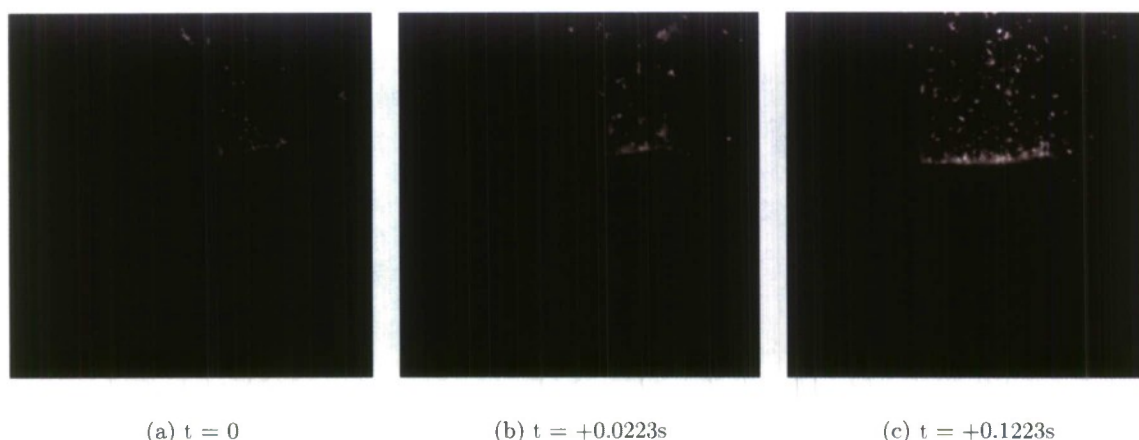


Figure 30: High Speed Imaging of Laser Ignition

pressures. Once complete, experimental efforts will move on to mimicking existing formulations [2] to determine repeatability, while continuing to perfect casting procedures in quartz tubes in preparation for characterization at high initial propellant temperatures and dynamic transient effects caused by CO<sub>2</sub> laser ignition. In addition to continuing high-speed imaging of laser ignition transients, work should continue with integration of the spectroscopy system and plans have been made to develop a control system for the CO<sub>2</sub> laser to generate variable pulse widths. Concurrently, progress should continue on further defining Series B propellants and re-evaluating Series A propellants at elevated temperatures to determine the temperature sensitivity of this formulation.

## References

1. Massa, L. and Jackson, T.L. Multidimensional numerical simulations of ammonium-perchlorate-based propellant combustion with fine/ultrafine aluminum. *Journal of Propulsion and Power*, 24(2):161-174 (2008).
2. Galfetti, L., DeLuca, L.T., Severini, F., Colombo, G., Meda, L. & Marra, G. Pre and post-burning analysis of nano-aluminized solid rocket propellants. *Aerospace Science and Technology*, 11:26-32 (2007).
3. Sutton, George P. and Biblarz, Oscar, *Rocket Propulsion Elements*, Wiley-Interscience, 2000.
4. Sambamurthi, Jayaraman, Price, E.W. and Sigman, R.K., Aluminum Agglomeration in Solid-Propellant Combustion, AIAA Vol. 22, No. 8, 1983.
5. M. Stephens, R. Carro, S. Wolf, T. Sammet, E. Petersen & C. Smith (2005) Performance of Ap-based composite propellant containing nano-scale aluminum. *AIAA Paper No. 2005-4470*, 41st AIAA/ASME/SAE/ASEE Joint Propulsion Conference & Exhibit, 10-13 July 2005, Tucson, Arizona.



6. Sammet, T. and Stephens, M. and Carro, R. and lePage, A. and Petersen, E., 43rd AIAA/ASME/ASME/SAE Joint Propulsion Conference and Exhibit, Cincinnati, OH, 2007, 2007.
7. Matthew [sic] Cliff, Ageing [sic] Characteristics of ALEX Nanosize Aluminum, AIAA Paper no. 2001-3287, 2001.
8. Jigatch, A.N., Leipunsky, I.O., Kuskov, M.L., Pshechenkov, P.A., Laritchev, M.N., Krasovsky, V.G. and Gogulya, M.F. , A Technique to Prepare Aluminized Nano-Sized Energetic Composition, AIAA Paper no. 2002-5735, 2002.
9. Dokhan, A., Price, E.W., Seitzman, J.M. and Sigman, R.K., Combustion Mechanisms of Bimodal and Ultra-Fine Aluminum in AP Solid Propellant, AIAA Paper no. 2002-4173, 2002.
10. Kuo, Kenneth K., Risha, Grant A. and Evans, Brian J. and Boyer, Eric, Potential Usage of Energetic Nano-sized Powders for Combustion and Rocket Propulsion, Materials Research Society, Vol. 800, 2004.
11. Kohga and Makato, Burning Rate Characteristics of Ammonium Perchlorate-Based Composite Propellant Using Bimodal Ammonium Perchlorate, Journal of Propulsion and Power, Vol. 24, No.3, 2008.
12. Jayaraman, K. and Anand, K.V. and Bhatt, D.S. and Chakravarthy, S.R. and Sarathi, R., Production, Characterization, and Combustion of Nano-Aluminum in Composite Solid Propellants, AIAA Paper no. 2007-1430, 2007.
13. Heister, S. and Austin, B.J. and Corpening, J. and Trebs, A. and Wernimont, E. and Linke, K., 2007.
14. Solid Propellant Processing Factors in Rocket Motor Design , NASA Report no. NASA-SP-8075, 1971.
15. Brewster, M.Q. & Parry, D.L. Radiative heat feedback in aluminized solid propellant combustion. *Journal of Thermophysics and Heat Transfer*, 2(2):123-130 (1988).
16. Modest, M.F. Radiative Heat Transfer, 2nd ed., Academic Press, New York (2003).
17. Jackson, T.L., Buckmaster, J. & Wang, X. The modeling of propellants containing ultrafine aluminum. *Journal of Propulsion and Power*, 23(1):158-165 (2007).
18. Massa, L., Jackson, T.L. & Buckmaster, J. Optimization of global kinetics parameters for heterogeneous propellant combustion using a genetic algorithm. *Combustion Theory and Modelling*, 11(4):553-568 (2007).
19. Hegab, A., Jackson, T.L., Buckmaster, J. and Stewart, D.S. Nonsteady burning of periodic sandwich propellants with complete coupling between the solid and gas phases. *Combustion and Flame*, 125:1055-1070 (2001).
20. Burke, S.P. and Schumann, T.E.W. Diffusion flames. *Industrial and Engineering Chemistry*, 20(8):998-1004 (1928).



21. Wang, X., Jackson, T.L., Bueckmaster, J., Massa, L. & Hossain, K. Three-dimensional modeling of aluminized composite solid propellant combustion. *AIAA Paper 2006-4927*, (2006).
22. Zhang, H. & Modest, M.F. Evaluation of the Planck-mean absorption coefficients from HITRAN and HITEMP databases. *Journal of Quantitative Spectroscopy and Radiative Transfer*, 73(6):649-653 (2002).
23. Najjar, F., Massa, L., Fiedler, R., Haselbacher, A. Wasistho, B. & Balachandar, S. Effects of aluminum propellant loading and size distribution in BATES motors: A multiphysics computational analysis. *AIAA Paper 2005-3997*, (2005).
24. Mench, M.M., Kuo, K.K., Yeh, C.L. & Lu, Y.C. Comparison of thermal behavior of regular and ultrafine aluminum powders (ALEX) made from plasma explosion process. *Combustion Science and Technology*, 135(1):269-292 (1998).
25. Jones, D.E.G., Brousseau, P., Fouehard, R.C., Tureotte, A.M. & Kwok, Q.S.M. Thermal characterization of passivated nanometer size aluminum powders. *Journal of Thermal Analysis and Calorimetry*, 61(3):805-818 (2000).
26. Bazyn, T., Krier, H. & Glumac, N. Shock tube measurements of combustion of nano-aluminum. *AIAA Paper 2006-1157*, (2006).
27. Aita, K., Glumac, N., Vanka, S.P. & Krier, H. Modeling the combustion of nano-sized aluminum particles. *AIAA Paper 2006-1156*, (2006).
28. Widener, J.F. & Beekstead, M.W. Aluminum combustion modeling in solid propellant combustion products. *AIAA Paper 98-3824*, (1998).
29. Massa, L., Jackson, T.L. and Bueckmaster, J. New Kinetics for a Model of Heterogeneous Propellant Combustion. *Journal of Propulsion and Power*, 21(5):914-924 (2005).
30. Massa, L., Jackson, T.L. and Short, M. Numerical Solution of Three-Dimensional Heterogeneous Solid Propellants. *Combustion Theory and Modelling*, 7(3):579-602 (2003).
31. Chen, M., Bueckmaster, J., Jackson, T.L. and Massa, L. Homogenization Issues and the Combustion of Heterogeneous Solid Propellants. *Proceedings of the Combustion Institute*, 29:2923-2929 (2002).
32. Jackson, T.L. and Bueckmaster, J. Heterogeneous Propellant Combustion. *AIAA Journal*, 40(6):1122-1130 (2002).
33. Brown, D. Traeger. Available at <http://www.eabrillo.edu/~dbrown/traeger/>, 2009.